Characterization of Novel III-V Semiconductor Devices

by

Sue Y. Young

B.S. Electrical Engineering
Massachusetts Institute of Technology 2005

Submitted to the Department of Electrical Engineering and Computer Science in partial fulfillment of the requirements for the degree of

Master of Engineering in Electrical Engineering and Computer Science

at the
MASSACHUSETTS INSTITUTE OF TECHNOLOGY

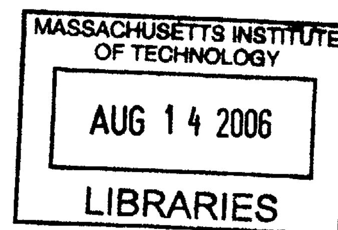
MASSACHUSETTS INSTITUTE OF TECHNOLOGY
AUG 14 2006
LIBRARIES

June 2006

© 2006 Massachusetts Institute of Technology. All rights reserved.

Author ....
Sue Y. Young
Department of Electrical Engineering and Computer Science
May 26, 2006

Certified by ....
...slie A. Kolodziejski
Professor of Electrical Engineering and Computer Science
...s Supervisor

Accepted by ....
...hur C. Smith
Chairman, Department Committee for Graduate Students

BARKER

Characterization of Novel III-V Semiconductor Devices

by

Sue Y. Young

Submitted to the Department of Electrical Engineering
and Computer Science on May 26, 2006 in partial fulfillment
of the requirements for the degree of
Master of Engineering in Electrical Engineering and Computer Science

ABSTRACT

This thesis presents the characterization of tunnel junctions and tunnel-junction-coupled lasers. The reverse-biased leakage current in a tunnel junction can be exploited to tunnel electrons from the valence band of one active region to the conduction band of a second active region. Thus, tunnel-junction-coupled lasers are highly efficient as they allow electrons to stimulate the emission of photons in more than one active region. The electrical characterization of InGaAs/GaAs tunnel junctions is presented. This thesis also gives an overview of the electrical and optical behavior of single-stage lasers as well as two-stage lasers coupled by InGaAs/GaAs tunnel junctions. Telecommunication applications motivated the use of InAs quantum dots and InAsP quantum dashes in the active layer design to provide near-infrared emission.

Thesis Supervisor: Leslie A. Kolodziejski
Professor of Electrical Engineering and Computer Science

Acknowledgements

First and foremost, I would like to thank Professor Leslie Kolodziejski for having faith in me from the moment I disclosed an interest in photonics, despite my inexperience and limited background. Needless to say, this year and this thesis would be impossible without her and her incredible guidance. Moreover, her commitment and dedication to her students, both as a teacher and as a supervisor, is so remarkable, and I am extremely thankful and privileged to have worked with her during my time at MIT.

This year would also not have been possible without the help of Dr. Gale Petrich. His constant insight and support were invaluable, and he never once hesitated to answer one of my many, many, many "quick questions," as trivial or long as they always were. I am so lucky to have collaborated with someone with such a devotion to and enthusiasm for great research.

I would especially like to give huge thanks to Dr. (forthcoming) Ryan D. Williams for being a fantastic officemate. Not only did he develop the foundation to this project and let me shadow him in the clean room, but he always listened to my stories and enlightened me on topics ranging from wedding registries to life as a grad student and everything in between.

I'd also like to thank Jim Daley in the Nanostructures Laboratory and Leo Missaggia at MIT Lincoln Laboratory who made it possible for these devices to even be tested, and my groupmates Reggie Bryant and Alex Grine for helping me out on the weekends. I am also grateful to all the students in the CIPS community who have entertained my questions, lent me equipment, and let me stand in their way. And, of course, I can also never thank Anne Hunter enough for her answers and support over the past five years.

I must also send love and thanks to all my friends who have made my transition out of college so easy and absolutely amazing. In particular, I'd like to thank my roommates for absurd and not-so-absurd sports, cooking spices, party themes, and unconditional support.

Most importantly, I'd like to thank my mom who is the best role-model, friend, mentor, and mother a daughter could ever dream of; my dad whose love, patience, and intellect I live to emulate; and my sister who is my best friend and whose advice, humor, and hugs I can't imagine life without.

THANKS!!!

Table of Contents

ABSTRACT 3

1.0 INTRODUCTION 15

2.0 TUNNEL JUNCTION DIODES 18

2.1 Background and Design Theory 18
- 2.1.1 What is a Tunnel Diode? 18
- 2.1.2 Design and Simulation 22

2.2 Research Approach 25
- 2.2.1 Research Objective 25
- 2.2.2 Fabrication Sequence 25
- 2.2.3 Testing Design 26

2.3 Results and Discussion 27
- 2.3.1 Ellipsometer Results 27
- 2.3.2 Fabrication Results 29
- 2.3.3 Electrical Results 31

3.0 QUANTUM DOT AND QUANTUM DASH LASERS 40

3.1 Background and Design Theory 40
- 3.1.1 Semiconductor Lasers 40
- 3.1.2 Laser Structures 45
- 3.1.3 Tunnel-Junction-Coupled Lasers 46
- 3.1.4 Quantum Dots 47
- 3.1.5 Quantum Dashes 48
- 3.1.6 Design of Quantum Dot Lasers 48
- 3.1.7 Design of Quantum Dash Lasers 50
- 3.1.8 Laser Fabrication 51

3.2 Research Approach 52
- 3.2.1 Research Objective 52
- 3.2.2 Laser Mounting Design 53
- 3.2.3 Electrical Testing Design 55

3.3 Results and Discussion 58
- 3.3.1 Packaging 58
- 3.3.2 Quantum Dots 59
- 3.3.3 Quantum Dashes 61
- 3.3.4 Future Work 61

4.0 SUMMARY 65

5.0 REFERENCES 68

6.0 APPENDIX 70

6.1 SimWindows Simulations 70
- 6.1.1 Device File 70

6.1.2 Material Parameters File 70
6.2 Variable Angle Spectroscopic Ellipsometry Results 75
6.2.1 5% Sample 75
6.2.2 10% Sample 76
6.2.3 15% Sample 77

List of Figures

FIGURE 1.1 Attenuation and dispersion in silica core fiber [3]. 16

FIGURE 1.2 Bandgap energy and lattice constant of III-V semiconductors at room temperature [3]. . 16

FIGURE 2.1 Band diagram and voltage-current response of a tunnel diode at equilibrium. 19

FIGURE 2.2 Band diagram and voltage-current response in forward bias at the point of maximum tunneling current. 19

FIGURE 2.3 Band diagram and voltage-current response under forward bias at the local current minimum. 20

FIGURE 2.4 Band diagram and voltage-current response under a large forward bias, inducing a thermal current. 20

FIGURE 2.5 Band diagram and voltage-current response under reverse-bias. 21

FIGURE 2.6 Structure of tunnel junction diode (not to scale), with Indium content (x) of 0%, 5%, 10%, and 15%. 22

FIGURE 2.7 Band diagram of an InGaAs tunnel diode for an Indium content of 0%, 5%, 10%, and 15%. 23

FIGURE 2.8 Effect of a -1V reverse bias and a +1V forward bias on a tunnel diode composed of $In_{0.15}Ga_{0.85}As$. 23

FIGURE 2.9 Simulated Zener breakdown of a GaAs tunnel diode. 24

FIGURE 2.10 Simulated forward tunneling characteristics of a GaAs tunnel diode. 24

FIGURE 2.11 Rapid thermal anneal sequence demonstrating the intermediate temperature stabilization steps. 26

FIGURE 2.12 Final structure of the tunnel junction diode. 26

FIGURE 2.13 Photograph of tunnel junction diode testing setup. 27

FIGURE 2.14 Variable angle spectroscopic ellipsometry testing setup. 28

FIGURE 2.15 Ellipsometry results for the MBE-grown tunnel junction diode with 5% Indium at an angle of 75 degrees. 28

FIGURE 2.16 VASE determined results, including the percentage of Indium (x) and the thicknesses of the layers in the tunnel junction. 29

FIGURE 2.17 Nomarski micrographs of the $In_{0.135}Ga_{0.865}As$ tunnel junction diode after etching the contacts. 30

FIGURE 2.18 Current response of a 6.5% Indium tunnel junction sample for various contact sizes. 31

FIGURE 2.19 Forward tunneling behavior for 6.5% Indium for various contact sizes. Inset shows the forward tunneling behavior normalized by contact area. 32

FIGURE 2.20 Reverse and forward bias current response, normalized by contact size, to an applied voltage. ... 33

FIGURE 2.21 A magnified view of the reverse bias current response, demonstrating a decrease in resistance for increasing Indium content. ... 34

FIGURE 2.22 Forward tunneling characteristics showing the trends in negative tunneling resistance as well as the peak and valley voltages and currents for increasing Indium content. ... 34

FIGURE 2.23 Normalized tunneling resistance for increasing Indium concentration. ... 36

FIGURE 2.24 Fitting the first term of Equation 2.1 to the experimental data by varying the peak voltage and peak current density to minimize the squared error. ... 37

FIGURE 2.25 The fitted values of the peak voltage and peak current. ... 37

FIGURE 2.26 Effect of annealing on reverse-biased tunneling resistance. ... 38

FIGURE 2.27 Temperature effect on reverse-biased tunneling resistance. ... 39

FIGURE 3.1 Three types of electron-photon interaction. ... 40

FIGURE 3.2 Fabry-Perot cavity and modes. ... 41

FIGURE 3.3 Optical gain and loss versus drive current density. ... 42

FIGURE 3.4 Relationship between the optical power generated for a given current injection. ... 43

FIGURE 3.5 The effect of temperature on optical power output and threshold current. ... 45

FIGURE 3.6 Tunnel-junction-coupled laser depicting how electron tunneling can stimulate emission in two lasers. ... 46

FIGURE 3.7 Density of states diagram for bulk, quantum well, and quantum dot structures. ... 47

FIGURE 3.8 Device structure of the quantum dot lasers. ... 49

FIGURE 3.9 Atomic force microscopy of gas source molecular beam epitaxially-grown InAs quantum dots [6] ... 50

FIGURE 3.10 Device structure of quantum dash laser. ... 50

FIGURE 3.11 Scanning electron micrograph (SEM) of the $InAs_{0.9}P_{0.1}$ quantum dashes grown using MBE. ... 51

FIGURE 3.12 Nomarski micrograph of the quantum dash laser (II). ... 52

FIGURE 3.13 Dimensions of copper mounts. ... 53

FIGURE 3.14 Structure of metals used to solder the GaAs or InP device to a copper mount. ... 54

FIGURE 3.15 Structure of metals used to solder the GaAs and InP devices to a CuW mount ... 55

FIGURE 3.16 Diagram of continuous operation testing using an InGaAs photodetector. ... 55

FIGURE 3.17 Wavelength detection range of an PbS detector [20] ... 56

FIGURE 3.18 Diagram of continuous or pulsed operation testing using an PbS photodetector. 56
FIGURE 3.19 Schematic of PbS detector circuit.. 57
FIGURE 3.20 Room temperature photoluminesence of quantum dot laser epilayer [20]........................ 58
FIGURE 3.21 Voltage characteristics of a single stage and two stage laser... 59
FIGURE 3.22 Output power for a single and two-stage laser. 60
FIGURE 3.23 Heating effects on output behavior due to slow continuous operation. 61
FIGURE 3.24 Structure of a stripe laser, demonstrating lateral current spreading. 62
FIGURE 3.25 Structure of a ridge laser with adequate lateral carrier confinement................................ 62

List of Tables

TABLE 1. Typical Parameters of Tunnel Diodes 22

TABLE 2. Final diameters of the contacts following the fabrication sequence 30

TABLE 3. Median experimental values of peak current, normalized peak current, valley current, normalized valley current, peak voltage, valley voltage, current ratio, and normalized minimum resistance for different percentages of Indium 35

TABLE 4. Impedance values for the PbS detector circuit. 57

TABLE 5. Lasing parameters of a 26.1 x 930 μm single-stage laser and a 26.7 x 1002 μm two-stage laser 60

1.0 INTRODUCTION

Semiconductor lasers play an essential role in a variety of fields, including medicine, atmospheric testing, manufacturing, and the entertainment industry. Additionally, highly-efficient laser diodes have revolutionized the telecommunication industry. Coupled with silica fibers, these devices are implemented in large-scale optical networks around the world. Compared to electrical-based telephony systems, photonic technology offers many benefits: higher bandwidth and thus higher information transmission rates; less interference from other electrical equipment and therefore lower crosstalk; good information retrieval; and parallel access of information. While metropolitan areas are connected together via optical networks, direct user connectivity is not yet as widely implemented due to higher costs, creating a bandwidth bottleneck for the user.

Fiber to the Home (FTTH) is one example of a point-to-multipoint network and telecommunication system that could potentially provide telephone, broadband internet and television to homes and businesses in one bundle. FTTH has already been implemented in countries in North America, Europe, the Middle East, and Asia. Japan leads the effort with 4.63 million connections as of March, 2006 [1]. The demand in the United States is quickly increasing as well; the Telecommunications Industry Association reported in April 2006 that 936 communities in 47 states offer FTTH broadband solutions, which includes a 107 percent increase in connections as of October 2005. Though costs still need to fall, global acceptance and demand are inevitably increasing [2].

One form of FTTH is based on a passive optical network (PON) which uses passive splitters to distribute fibers to individuals, eliminating the need for neighborhood electrical equipment. The PON uses wave-division multiplexing (WDM) such that three streams of data are sent on a single fiber: telephone, internet, and video services are received at 1490 nm and 1550 nm, and data is transmitted at 1310 nm.

High-efficiency lasers at these wavelengths are desired as they offer minimal dispersion in optical fibers. As shown in Figure 1.1, attenuation is minimized at 1550 nm, and dispersion is minimized at 1300 nm. However, Figure 1.2 demonstrates that no binary material system has the corresponding bandgap energy to emit at these wavelengths.

FIGURE 1.1 Attenuation and dispersion in silica core fiber [3].

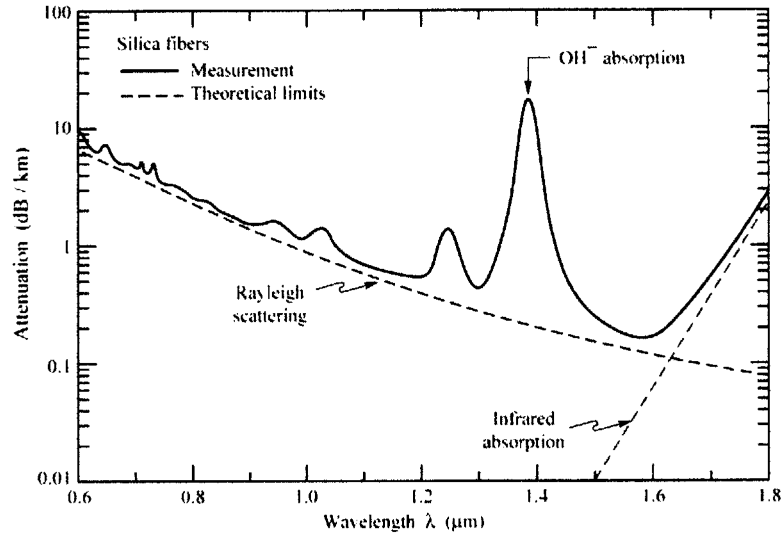

FIGURE 1.2 Bandgap energy and lattice constant of III-V semiconductors at room temperature [3].

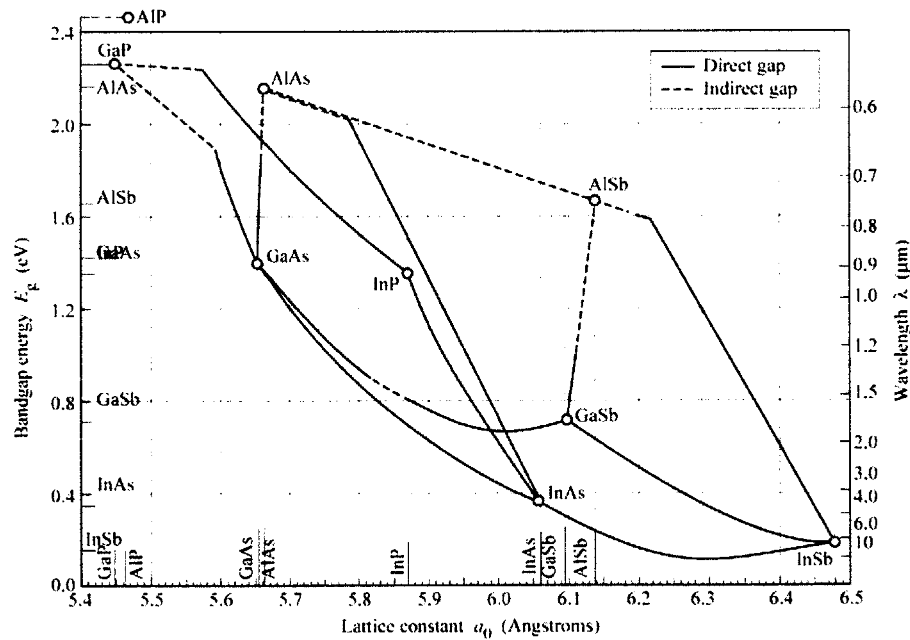

One of the technologies developed to provide 1300 nm emission involves the use of InAs quantum dots on GaAs wafers in which the Stranski-Krastanov growth of InAs on GaAs is exploited. This technology has also been expanded to other wavelengths. Specifically, InAs-based quantum dashes, which are elongated quantum dots, on InP-based material alter the bandgap such that these lasers will be able to emit wavelengths between 1500 nm to 1800 nm.

Nonetheless, a limiting factor that all semiconductor lasers in these applications share is that one electron can release at most one photon. High-efficiency lasers are often desired as they consequently offer higher output powers and lower threshold currents.

Circumnavigating the injection current efficiency limit is possible by incorporating a tunnel junction. Fabricating lasers in series via a tunnel junction diode can dramatically increase the lasing efficiency.

Therefore, cascading lasers together with tunnel junctions allow multiple photon emission for every electron, while the use of quantum dots and dashes expand the wavelength emission range in the near-infrared region. Chapter 2 will investigate the behavior of InGaAs tunnel junction diodes for different percentages of Indium. A low resistance tunnel junction would increase the tunneling of electrons and thus the quantum efficiency of a device incorporating the tunnel junction. Chapter 3 will characterize single stage GaAs-based quantum dot lasers, tunnel-junction-coupled quantum dot GaAs-based lasers incorporating Indium tunnel junctions, and InP-based quantum dash lasers. Chapter 4 summarizes the overall results and comments on future directions.

2.0 TUNNEL JUNCTION DIODES

As optical transmitters, semiconductor lasers often require high output powers with low threshold currents. However, most lasers are inherently limited to 100% injection current efficiency, where one photon is emitted for every electron. Fortunately, cascade lasers overcome the maximum quantum efficiency of a single laser; in a cascade laser, individual lasers are placed in series with each other so that a single electron can flow through and stimulate emission in each device. The differential efficiency, given by the amount of light emitted over current, increases by the number of stacked stages.

Electrically connecting individual laser diodes in series suffers from many parasitic impedances and is hard to couple into a single fiber. As a result, the overall performance of the system is significantly reduced. Connecting the lasers in series during the epitaxial growth process provides an excellent alternative and is accomplished with a Tunnel Junction. [4]

A tunnel junction works by simply exploiting the reverse-biased leakage current of a highly-reversed biased heavily-doped diode. Coupled between the two lasers, the tunnel junction diode allows an electron to tunnel from the valence band of the first laser, after stimulating emission, to the conduction band of the second laser.

This chapter introduces and characterizes InGaAs tunnel diodes. The incorporation of Indium can lower the bandgap and effectively improve the tunneling performance of the device.

2.1 Background and Design Theory

2.1.1 What is a Tunnel Diode?

The tunnel diode is a typical p-n junction with the exception that both the p-side and n-side of the device are degenerately-doped. As a result, the Fermi-levels are located within the conduction band for the n-type material and within the valence band for the p-type material.

Figure 2.1 shows the band diagram and electrical characteristics of a highly degenerately-doped diode at equilibrium with no net current flow. When a forward bias is applied, a net current from the n- to the p-side occurs. The quasi-Fermi level of the n-doped side increases with respect to the p-doped side and electrons consequently tunnel to the p-doped side of the device, increasing the current.

FIGURE 2.1 Band diagram and voltage-current response of a tunnel diode at equilibrium.

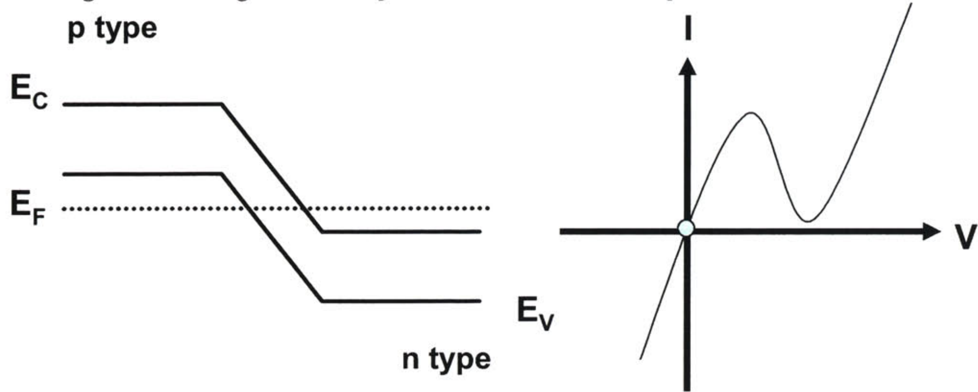

Eventually, the tunnel current reaches a local peak when the maximum number of occupied states in the conduction band on the n-side is aligned with the maximum number of unoccupied states in the valence band on the p-side. This is shown in Figure 2.2. Increasing the forward bias further brings the n-side conduction band and the p-side valence band gradually out of alignment and reduces the current. The point of local minimum is shown in Figure 2.3 and depicts the point at which the occupied and unoccupied states are no longer aligned. Ideally, the current should go to zero, as tunneling across the junction is no longer possible. However, an excess current exists; electrons tunnel via energy levels within the bandgap due to the spread in the dopant impurity ionization energy and indirect tunneling.

FIGURE 2.2 Band diagram and voltage-current response in forward bias at the point of maximum tunneling current.

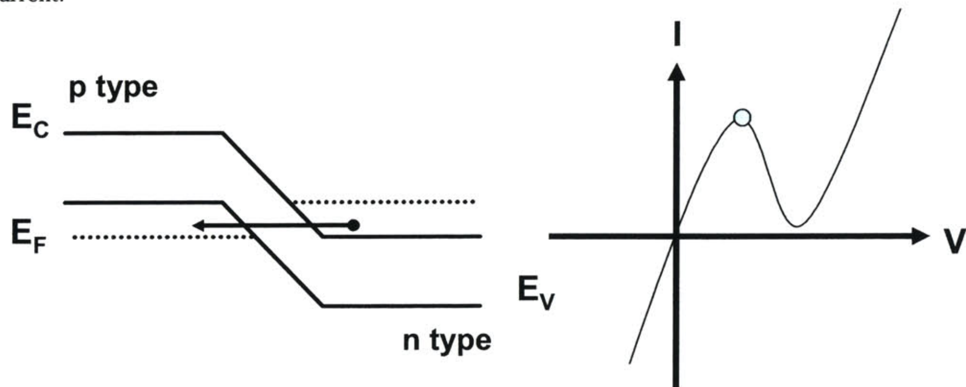

FIGURE 2.3 Band diagram and voltage-current response under forward bias at the local current minimum.

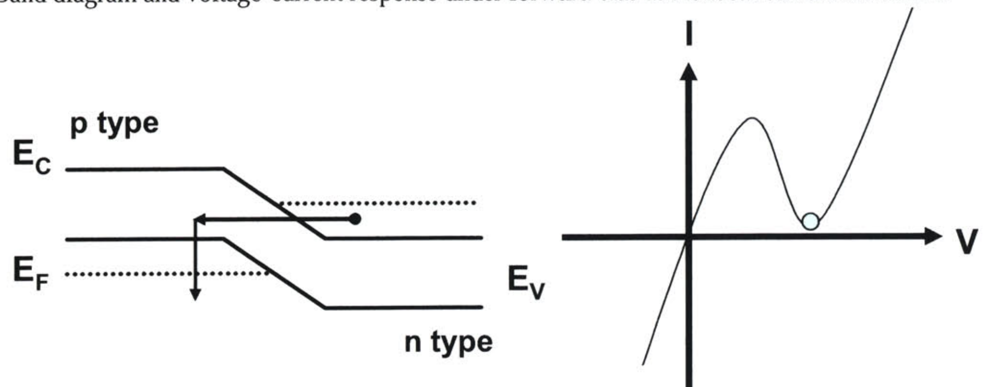

Further increasing the forward bias, the tunnel junction device begins to behave similar to a regular p-n diode. Electrons and holes are injected over their respective barriers, resulting in the diffusion of minority carriers typically seen in a normal p-n junction. This current is demonstrated in Figure 2.4.

FIGURE 2.4 Band diagram and voltage-current response under a large forward bias, inducing a thermal current.

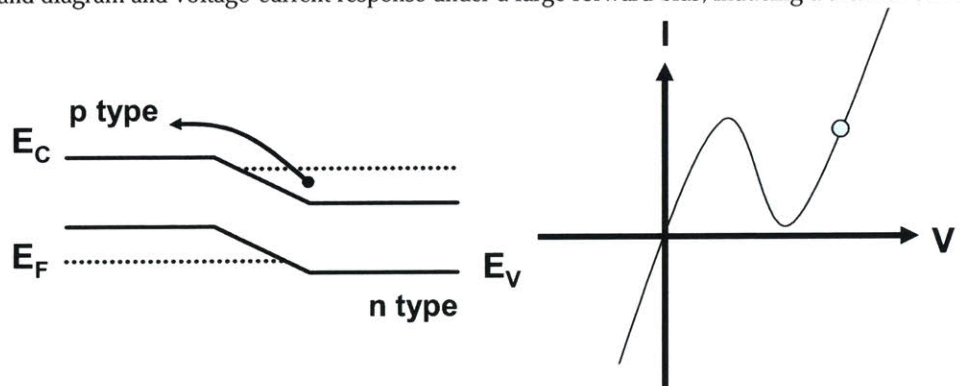

FIGURE 2.5 Band diagram and voltage-current response under reverse-bias.

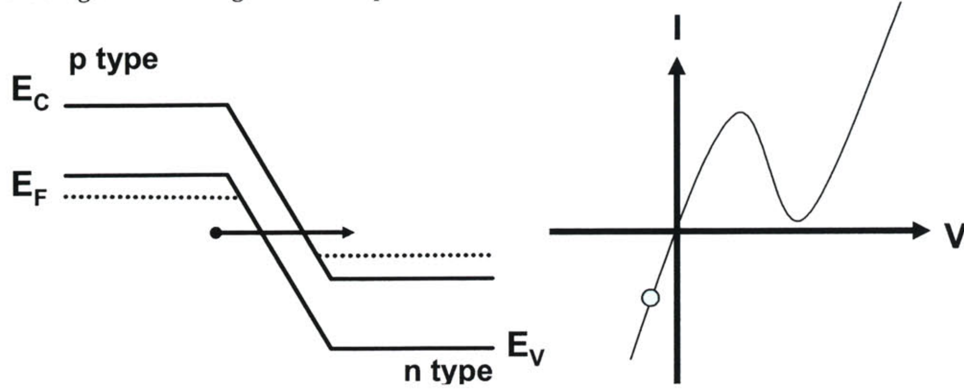

Figure 2.5 shows the device in reverse bias. Raising the p-side quasi-Fermi level above the n-side quasi-Fermi level promotes the tunneling of electrons from the occupied states in the valence band on the p-side to the empty states in the conduction band on the n-side. Increasing the negative bias further increases the negative tunneling current. This phenomenon of Zener tunneling, where electrons can move from the valence band of one device to the conduction band of the next, allows semiconductor lasers to be connected epitaxially in series.

Given an applied voltage, the current in a tunnel diode is given by

$$I = I_P \cdot \left(\frac{V}{V_P}\right) \cdot \exp\left(1 - \frac{V}{V_P}\right) + I_O \cdot \exp\left(1 - \frac{qV}{kT}\right) + I_{excess} \quad \textbf{(EQ 2.1)}$$

where the first term models the tunneling current, where I_P and V_P are the peak current and peak voltage, respectively. The second term explains the behavior seen in a simple diode, modeling the current due to the diffusion and drift of minority carriers. The tunneling resistance can be obtained from the first part of Equation 2.1 and is given in Equation 2.2.

$$R = \left(\frac{dI}{dV}\right)^{-1} = -\left[\left(\frac{V}{V_P} - 1\right) \cdot \frac{I_P}{V_P} \cdot \exp\left(1 - \frac{V}{V_P}\right)\right]^{-1} \quad \textbf{(EQ 2.2)}$$

When the tunnel diode is forward biased, the point at which the negative slope is maximum gives the minimum negative resistance. This value can be approximated as follows:

$$|R_{min}| \approx \frac{2V_P}{I_P} \quad \textbf{(EQ 2.3)}$$

This negative resistance is often exploited for switching, amplification, and oscillation purposes, and therefore implemented in high speed switching circuits and microwave amplifiers and oscillators. Typical values of the peak-to-valley current ratio (I_P/I_V), the

peak voltage (V_P), and the valley voltage (V_V) of Ge, Si, and GaAs tunnel diodes are listed in Table 1. [5]

TABLE 1. Typical Parameters of Tunnel Diodes.

Semiconductor	I_P/I_V	V_P (V)	V_V (V)
Ge	8	0.055	0.35
Si	3.5	0.065	0.42
GaAs	15	0.15	0.5

2.1.2 Design and Simulation

The incorporation of Indium in a GaAs tunnel diode has the potential to further increase the tunneling current in the device by decreasing the bandgap. Figure 2.6 depicts a simple degenerately-doped p-n junction diode.

FIGURE 2.6 Structure of tunnel junction diode (not to scale), with Indium content (x) of 0%, 5%, 10%, and 15%.

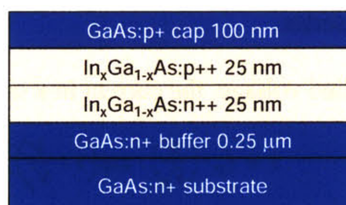

Degenerate doping is required to move the quasi-Fermi levels of the diodes into the conduction and valence bands. The device was grown using a Gas-Source Molecular Beam Epitaxy (GSMBE) system. The epilayer structure was grown at a rate of approximately 0.5 μm/hour and at a substrate temperature of 480°C. Hall measurements of heavily n- and p-type doped GaAs, using Si and Be as dopants, confirmed high doping concentrations of approximately 1×10^{19} cm^{-3}. The desired Indium content for the tunnel junctions were 0%, 5%, 10%, and 15%. [6]

Figure 2.7, shows the band diagrams of the InGaAs tunnel diode at equilibrium with an Indium content of 0%, 5%, 10%, and 15%. The device is sandwiched between doped GaAs. As the Indium content is increased, the decrease in bandgap is clearly demonstrated. The jumps at the junction interfaces are attributed to the slight inconsistencies between the GaAs material model and the InGaAs material model. Material parameter files and device files can be found in Appendix 6.1.

FIGURE 2.7 Band diagram of an InGaAs tunnel diode for an Indium content of 0%, 5%, 10%, and 15%.

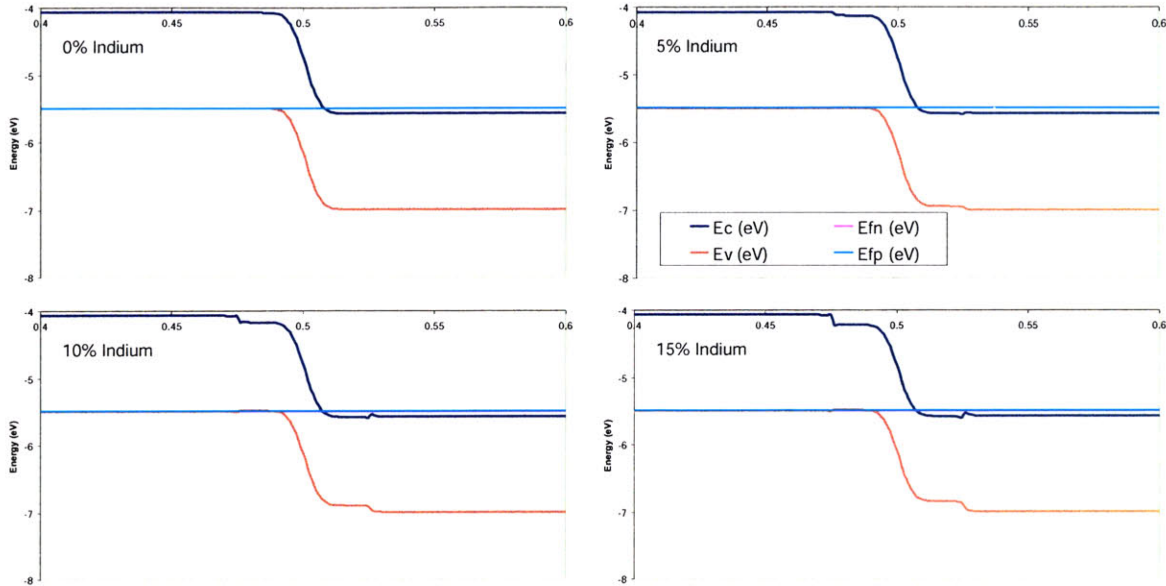

Figure 2.8 shows the effect of a forward and reverse bias on the band structure. The diffusion of minority carriers occur with a positive applied bias. With a negative applied bias, the quasi-Fermi levels are now aligned such that tunneling is encouraged.

FIGURE 2.8 Effect of a -1V reverse bias and a +1V forward bias on a tunnel diode composed of $In_{0.15}Ga_{0.85}As$.

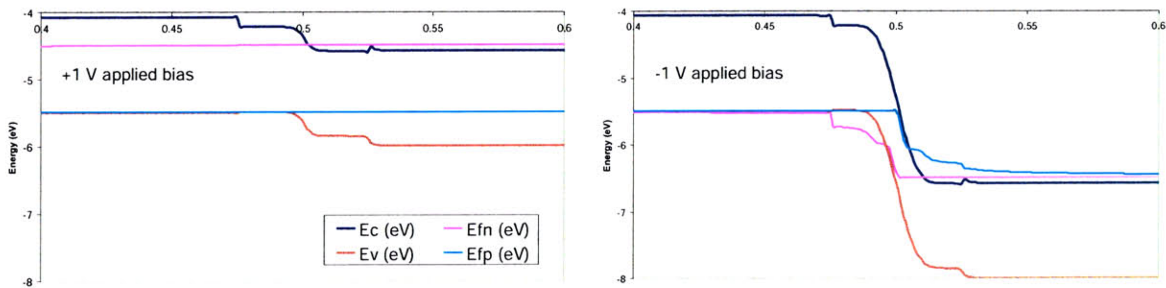

The effect of the reduced bandgap can be directly demonstrated by plotting the tunneling current response of the tunnel diode given an applied bias. Figure 2.9 and 2.10 simulates the current density response for a given applied voltage. Figure 2.9 shows the Voltage-Current behavior of GaAs tunnel diode, clearly demonstrating a Zener tunneling current. A closer view of the origin in Figure 2.10 depicts the forward tunneling current.

FIGURE 2.9 Simulated Zener breakdown of a GaAs tunnel diode.

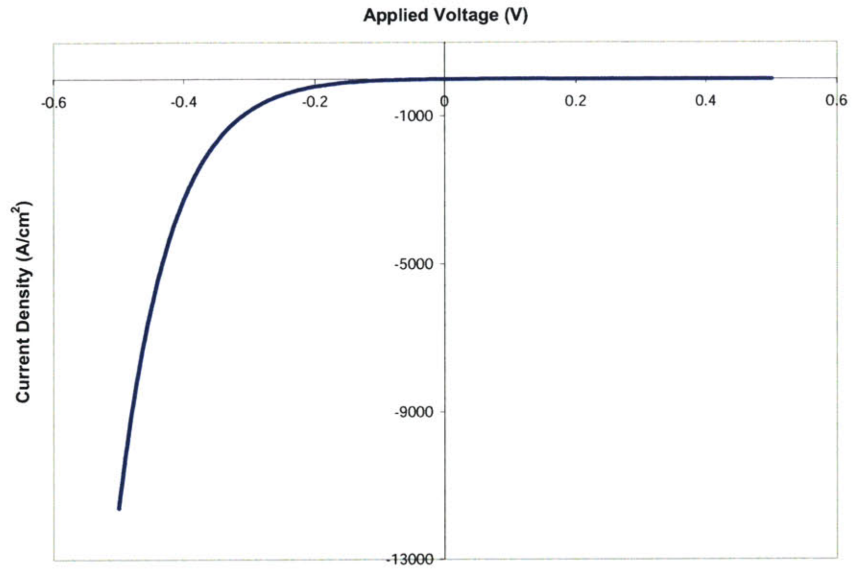

FIGURE 2.10 Simulated forward tunneling characteristics of a GaAs tunnel diode.

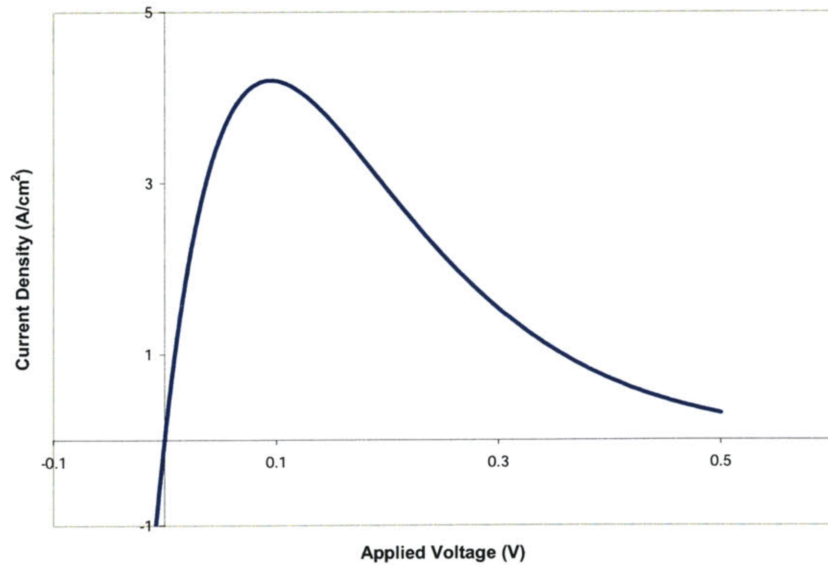

The first term in Equation 2.1 is used to plot the tunneling characteristics in both figures. V_P can be calculated from

$$V_P \approx \frac{\phi_n + \phi_p}{3} \quad \text{(EQ 2.4)}$$

where ϕ_n is the degeneracy on the n side and is given by

$$\phi_n \approx \frac{kT}{q} \cdot \left[\ln\left(\frac{N_D}{N_C}\right) + 0.35 \cdot \left(\frac{N_D}{N_C}\right)\right] \quad \text{(EQ 2.5)}$$

where N_D is the donor concentration and N_C is the effective density of states at the conduction band edge. Similarly, ϕ_p is the degeneracy on the p-side and can be calculated by equation 2.5, where N_D and N_C are respectively replaced with N_A, the acceptor concentration, and N_V, the effective density of states at the valence band edge. For GaAs with a n- and p-type doping of 1 x 10^{19} cm^{-3}, the peak voltage for a 0% Indium tunnel diode is 0.095V. An experimental value of 4.2 A/cm^2 is used as the peak current density in Figure 2.9 and 2.10, as previously determined for a GaAs tunnel diode in [7].

2.2 Research Approach

2.2.1 Research Objective

Our goal is to electrically characterize the tunneling behavior of the InGaAs/GaAs structures. The ideal performance of the devices would not only demonstrate tunneling behavior but also demonstrate a decrease in resistance as the concentration of Indium is increased in the tunnel junction.

2.2.2 Fabrication Sequence

To effectively test the wafer structure previously outlined in Section 2.1.2, appropriate contacts are necessary. A mask with circles varying in diameter from 17.5 to 90 μm is used to create contact pads of different sizes. The metal contacts consisting of Ti/Pt/Au (300/200/2500Å) were defined using a lift-off process. A 30 second wet etch using NH_4:H_2O_2:DI (10:5:240) isolates the individual tunnel junction devices from each other. The wet etch etches through the upper GaAs layer and through the InGaAs layers to create well defined tunnel junctions. Ti/Pt/Au can form an ohmic contact to both n-type and p-type GaAs, so a back-side metal contact consisting of Ti/Pt/Au of the same thickness as the top contact is deposited, followed by a rapid thermal anneal (RTA) for 30 seconds at 380°C. The RTA consists of ramping steps and intermediate temperature stabilization and is modeled in Figure 2.11. The final device structure is shown in Figure 2.12.

FIGURE 2.11 Rapid thermal anneal sequence demonstrating the intermediate temperature stabilization steps.

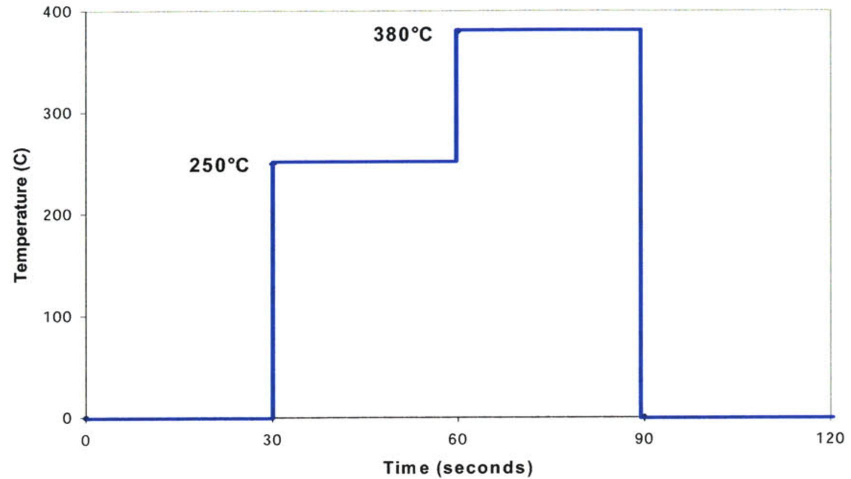

FIGURE 2.12 Final structure of the tunnel junction diode.

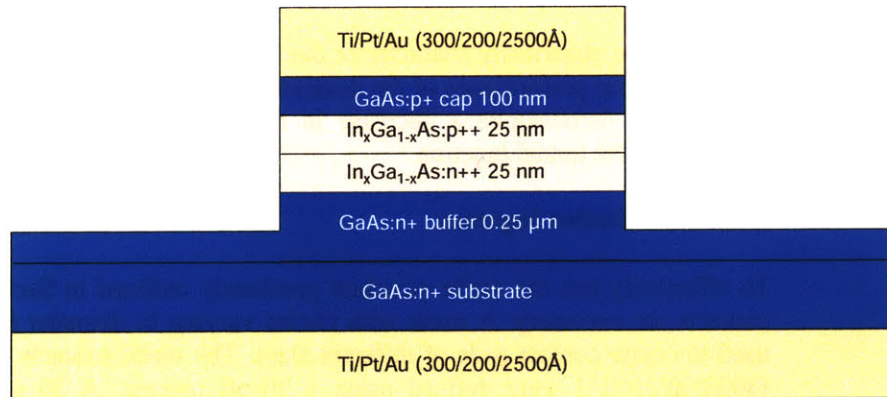

Photolithography is performed in the Microsystems Technology Laboratory with the help of Ryan D. Williams. All of the subsequent fabrication steps are performed in the Nanostructures Laboratory with the assistance of Ryan D. Williams. Metallization is carried out by James Daley.

2.2.3 Testing Design

To characterize the InGaAs/GaAs tunnel junctions, voltage-current performance of the device is required. A semiconductor parameter analyzer is used to measure the output current for a given applied bias. Figure 2.13 shows a photograph of the testing apparatus.

FIGURE 2.13 Photograph of tunnel junction diode testing setup.

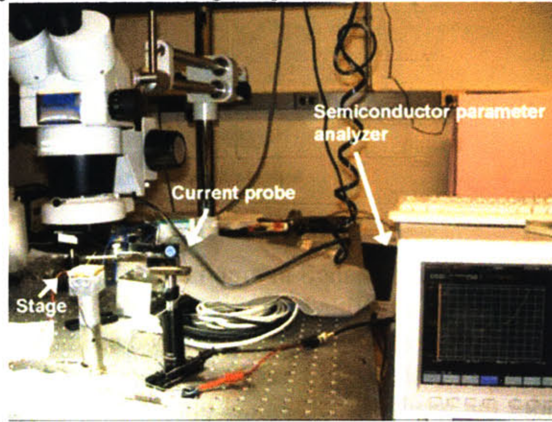

A voltage sweep from -500 mV to +500 mV is applied to the various sized contacts. Thus, the resistance for different concentrations of Indium and for different contact sizes can be calculated. The resistance should decrease for increasing pad size and decrease for increasing Indium concentrations. Forward tunneling parameters, including peak and valley voltages and currents, can also be obtained from the data. The effect of the final RTA step in the fabrication sequence and the effect of changes in temperature will also be analyzed.

2.3 Results and Discussion

2.3.1 Ellipsometer Results

Various tunnel junctions were designed and grown to have an Indium content of 0%, 5% 10%, and 15%. Before device fabrication, the exact alloy percentage is first assessed using variable angle spectroscopic ellipsometry (VASE). As shown in Figure 2.14, the ellipsometer shines polarized light onto the sample and measures the change in polarization caused by the structure's index of refraction to determine the thickness and composition of each layer in the structure. Ellipsometer measurements were taken of the MBE-grown wafers with 5%, 10%, and 15% Indium at three angles of incidence: 65, 70, and 75 degrees. The analyzer was moved to the same angle as the light source.

FIGURE 2.14 Variable angle spectroscopic ellipsometry testing setup.

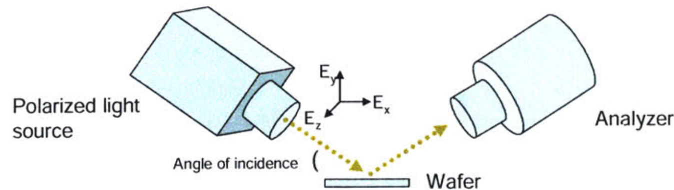

At each angle, the change in amplitude, *tan*(Ψ), and phase, *cos*(Δ), of the incident light were measured and fitted. Figure 2.15 depicts the experimental results as well as the model fit for the structure with a designed 5% Indium tunnel junction at a measured angle of 75 degrees, showing a very close model fit to the ellipsometer data. Appendix 6.2 includes the results for all tunnel junction samples at all three angles. The VASE model that was used to fit the data is based on the design structure as outlined in Figure 2.6 as well as an additional top layer of GaAs oxide resulting from the wafer's exposure to air. The curve fitting program uses $\Psi(\lambda, \theta)$ and $\Delta(\lambda, \theta)$ to determine the thickness and composition of each layer of the dielectric stack.

FIGURE 2.15 Ellipsometry results for the MBE-grown tunnel junction diode with 5% Indium at an angle of 75 degrees.

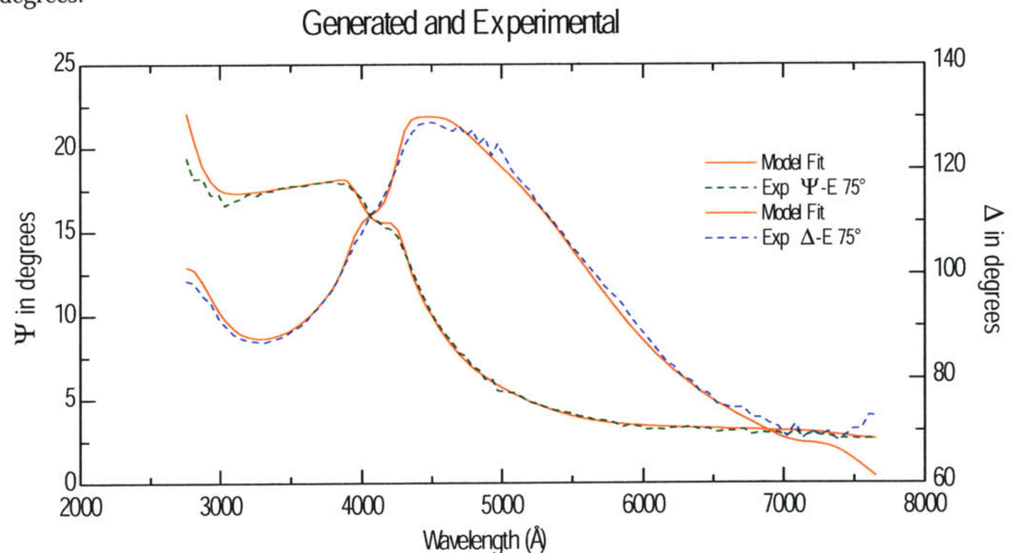

For each sample wafer, $\Psi(\lambda, \theta)$ and $\Delta(\lambda, \theta)$ were measured and fitted for angles of incidence of 65, 70, and 75 degrees. The three sets of data were used to determine the GaAs thickness, the InGaAs composition and thickness, and the native GaAs oxide thickness for each wafer. Figure 2.16 shows the results determined by the ellipsometer data.

FIGURE 2.16 VASE determined results, including the percentage of Indium (x) and the thicknesses of the layers in the tunnel junction.

3 gaas-ox	2.3546 nm
2 gaas	99.248 nm
1 ingaas x=0.065	57.854 nm
0 gaas	0.3 mm

3 gaas-ox	2.2666 nm
2 gaas	102.82 nm
1 ingaas x=0.115	59.84 nm
0 gaas	0.3 mm

3 gaas-ox	2.1751 nm
2 gaas	105.4 nm
1 ingaas x=0.135	59.917 nm
0 gaas	0.3 mm

The GaAs capping layer is within 5% of its designed thickness, and the tunnel junction layers are all within 20% of their designed thicknesses. The native oxide layer is small and can be removed with an initial oxide etch. Indium contents were found to be 6.5%, 11.5%, and 13.5%. These Indium compositions will be used in the analysis of the InGaAs tunnel diodes.

2.3.2 Fabrication Results

The following fabrication sequence, as outlined in Section 2.2.2 was performed on the tunnel junction diodes with 0%, 6.5%, and 11.5% Indium:

- Photolithography using image reversal resist
- Deposition of Ti/Pt/Au (300/200/2500Å)
- Metal lift-off
- 30 second NH_4:$H2O_2$:DI (10:5:240) etch
- Back-side deposition of Ti/Pt/Au (300/200/2500Å)
- RTA for 30 seconds at 380°C

The $In_{0.135}Ga_{0.865}As$ tunnel junction diode followed the same fabrication sequence but instead underwent a 60 second NH_4:H_2O_2:DI (10:5:240) wet etch. The 30 second etch etched 225 nm while the 60 second etch etched 445 nm. Figure 2.17 shows this sample after the etch. Etching of the 0%, 6.5%, and 11.5% diodes displayed similar results.

FIGURE 2.17 Nomarski micrographs of the $In_{0.135}Ga_{0.865}As$ tunnel junction diode after etching the contacts.

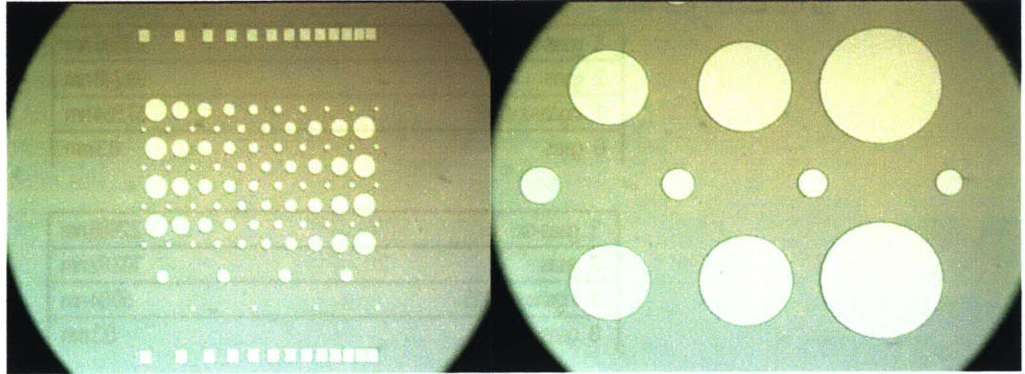

The size of the circle contacts were measured using a Nomarski microscope. The final diameters are listed in Table 2.

TABLE 2. Final diameters of the contacts following the fabrication sequence.

Desired diameter (μm)	Actual diameter (μm)
90	88.74
70	66.56
60	57.42
50	48.29
40	39.15
35	33.93
30	28.71
25	23.49
20	20.88
17.5	18.27

Thus, the fabrication of the tunnel junction diodes was successful, giving near perfect contact diameters with clean etches.

2.3.3 Electrical Results

Results by Contact Size

The testing setup as described in Section 2.2.3 was used to measure the current response of the tunnel junction diodes for a given applied voltage. A voltage sweep from -500 mV to +500 mV (10 mV steps) was applied to the contacts of diameters varying from 90 µm down to 35 µm. Measurements of the current response from the smaller contacts were difficult to obtain due to the poor contact between the wafer and the current probe. Figure 2.18 shows the voltage-current characteristics for the 6.5% Indium tunnel junction diode. As demonstrated, multiple measurements were taken, and trend lines demonstrate general consistency between the measurements. A decrease in resistance for increasing contact size is clearly demonstrated. The results of multiple measurements for the 0%, 11.5%, and 13.5% Indium tunnel junctions showed an identical trend in tunneling behavior: an increase in contact size decreased the tunneling resistance. More importantly, all of the results demonstrate the current-voltage response of a tunnel diode as discussed in Section 2.1.1.

FIGURE 2.18 Current response of a 6.5% Indium tunnel junction sample for various contact sizes.

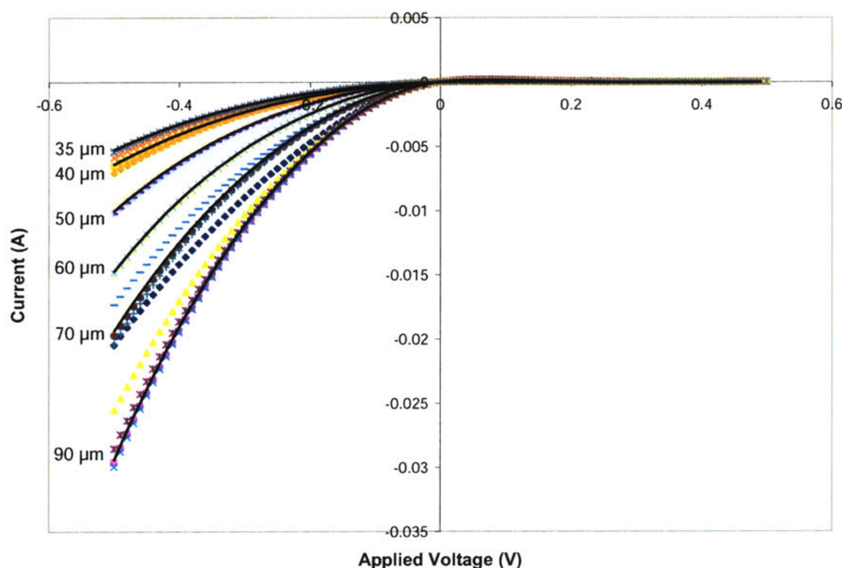

A closer look at the forward tunneling characteristics for the 6.5% Indium tunnel junction device is shown in Figure 2.19. The peak and valley behavior of a tunnel diode, as previously discussed in Section 2.1.1, is demonstrated. Also, the inset in Figure 2.19 shows the forward tunneling behavior normalized for area; the overlap of the data indicates consistency across the wafer. Again, data for the 0%, 11.5%, and 13.5% Indium tunnel junctions gave very similar results. Therefore, further discussion on the electrical characterization of the tunnel diodes will focus on the current density behavior unless otherwise noted.

FIGURE 2.19 Forward tunneling behavior for 6.5% Indium for various contact sizes. Inset shows the forward tunneling behavior normalized by contact area.

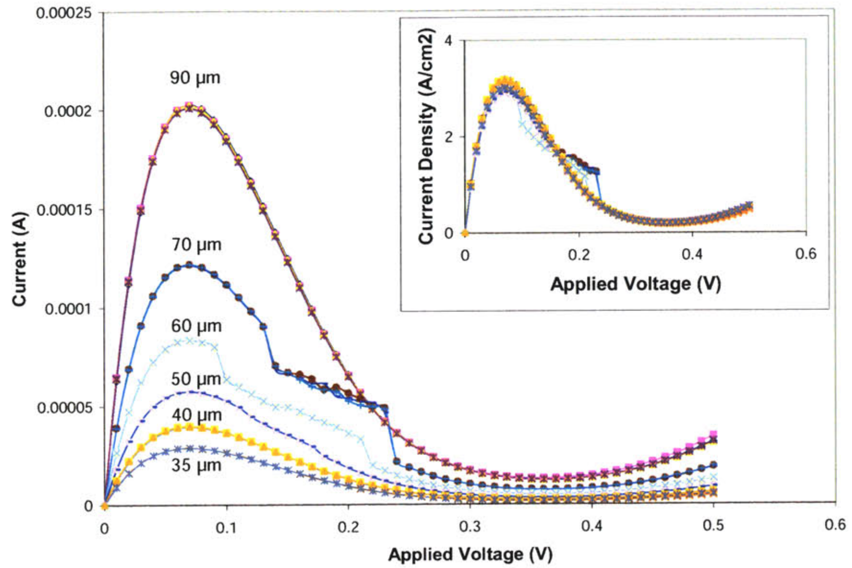

Indium Effects on Tunneling

For all of the devices, over 250 measurements were taken. Compilation of the results at each Indium content was done by calculating the medium current density response for each device. Figure 2.20 plots the response of current density to the applied voltage for tunnel junctions with 0%, 6.5%, 11.5%, and 13.5% Indium.

FIGURE 2.20 Reverse and forward bias current response, normalized by contact size, to an applied voltage.

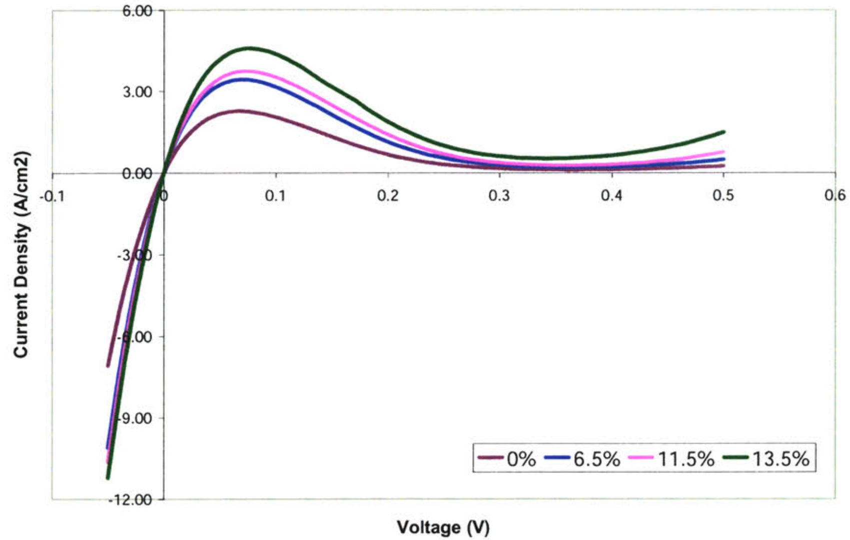

Tunnelling behavior, as previously predicted theoretically, is demonstrated under reverse and forward bias. Moreover, under forward bias, the tunneling current first peaks but is then followed by a brief range of negative resistance until the thermal current begins to dominate with the forward injection of minority carriers.

Figure 2.21 shows the complete reverse-biased behavior. The tunneling resistance decreases as the Indium percentage increases; more electrons tunnel through the junction at a given applied bias, as expected for a smaller bandgap. Significantly, when implemented in a tunnel-junction-coupled laser, a smaller tunneling resistance would yield a more efficient laser.

FIGURE 2.21 A magnified view of the reverse bias current response, demonstrating a decrease in resistance for increasing Indium content.

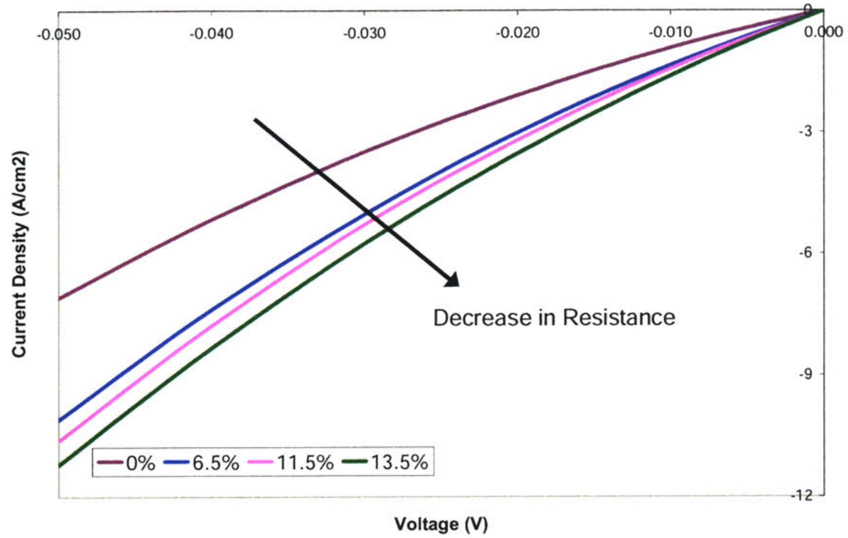

Figure 2.22 confirms the tunneling behavior in the forward-biased region. The figure also demonstrates the trends of the device parameters, which are listed in Table 3. The peak voltage increases, though slightly, while the valley voltage decreases.

FIGURE 2.22 Forward tunneling characteristics showing the trends in negative tunneling resistance as well as the peak and valley voltages and currents for increasing Indium content.

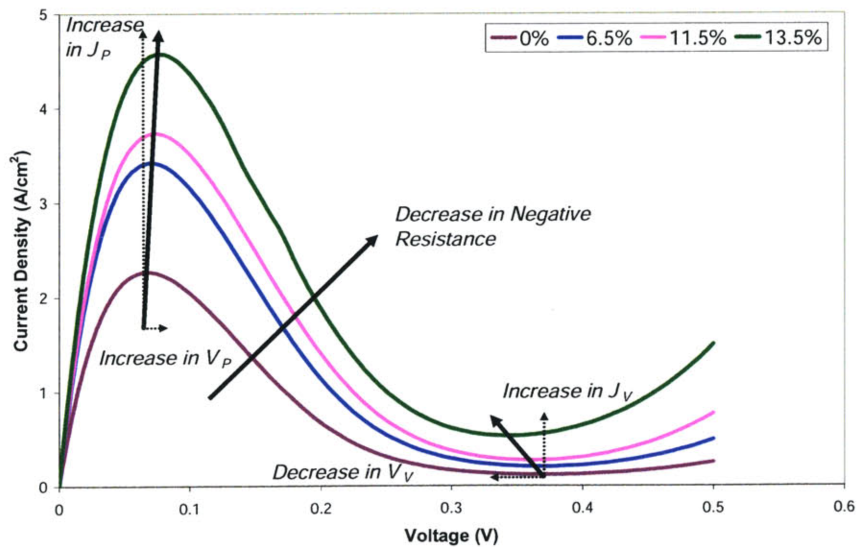

TABLE 3. Median experimental values of peak current, normalized peak current, valley current, normalized valley current, peak voltage, valley voltage, current ratio, and normalized minimum resistance for different percentages of Indium.

Percentage of Indium	Ip (A)	Jp (A/cm2)	Iv (A)	Jv (A/cm2)	Vp (V)	Vv (V)	Ip/Iv	Normalized R (Ω*cm2)
0.00%	9.29E-05	2.26	4.86E-06	0.12	0.07	0.37	19.2	1.19
6.45%	1.32E-04	3.43	7.86E-06	0.20	0.07	0.37	16.7	0.69
11.50%	1.62E-04	3.68	1.15E-05	0.27	0.07	0.36	13.6	0.51
13.50%	2.90E-04	4.56	2.83E-05	0.44	0.08	0.36	10.0	0.34

From Table 3, the difference between the peak and valley voltage is 0.3 V for 0% Indium, which is very close to the value of 0.35 V listed in Table 1 as a typical device parameter of a GaAs tunnel diode. Table 1 also listed a peak-to-valley ratio for GaAs of 15, close to the experimentally determined value.

Also notable is the rise in the valley current as the percentage of Indium is increased. One possible explanation is an increase in excess current by means of electrons tunneling through the forbidden bandgap. The incorporation of Indium might have increased the number of indirect states. Also likely is that the net flow of minority carriers occurs at a lower voltage, lifting the value of valley current. This is expected as increasing the percentage of Indium decreases the bandgap and the effective voltage at which the thermal current begins to dominate.

Additionally, the increase in slope as the quantity of Indium is increased indicates a decrease in resistance. The minimum negative resistance, as calculated from Equation 2.3, are included in Table 3 and plotted in Figure 2.23. A clear linear inverse relationship is demonstrated between Indium content and tunneling resistance.

FIGURE 2.23 Normalized tunneling resistance for increasing Indium concentration.

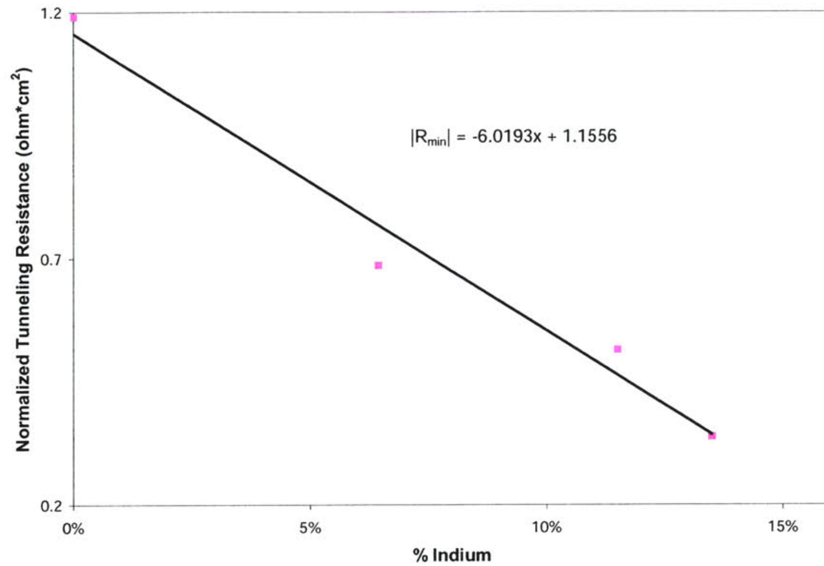

Parameter Modeling

In addition to simply extracting the tunneling parameters, the tunneling parameters were determined by fitting the first term of Equation 2.1 to the experimental data close to the point of zero bias, from -70 mV to + 70 mV, by varying the peak current and voltage values. The fitting results are shown in Figure 2.24 and indicate a very close fit to the experimental data. The values for peak voltage and peak current were determined by minimizing the squared error between the two plots. The extracted parameter values are plotted in Figure 2.25. As the model for tunneling current is primarily dependent on these two parameters, as suggested by Equation 2.1, an increase in both of these values would increase the tunneling current. Both of these trends are clearly demonstrated.

FIGURE 2.24 Fitting the first term of Equation 2.1 to the experimental data by varying the peak voltage and peak current density to minimize the squared error.

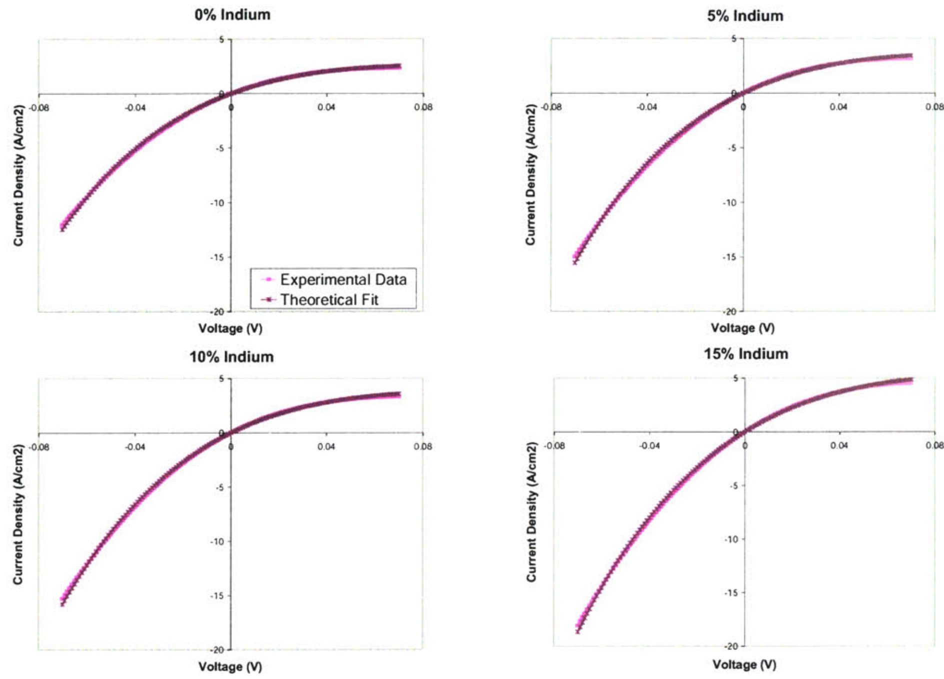

FIGURE 2.25 The fitted values of the peak voltage and peak current.

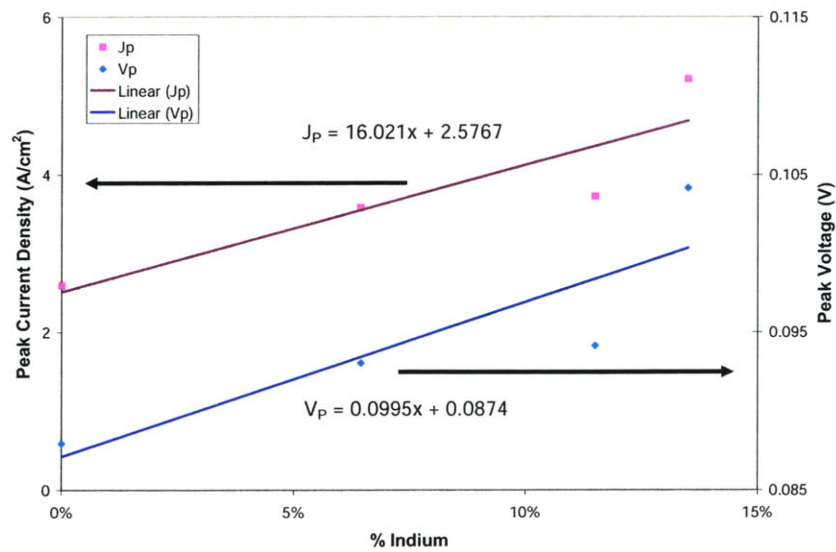

Effects of Annealing

Electrical characterization of the 13.5% Indium tunnel diode was performed before and after the final annealing step. All tests were preformed on a 90 μm contact, and Figure 2.26 shows the un-normalized result: annealing the device significantly decreases the resistance of the tunnel diode. Thus, the anneal is effective in alloying the metal-semiconductor interface.

FIGURE 2.26 Effect of annealing on reverse-biased tunneling resistance.

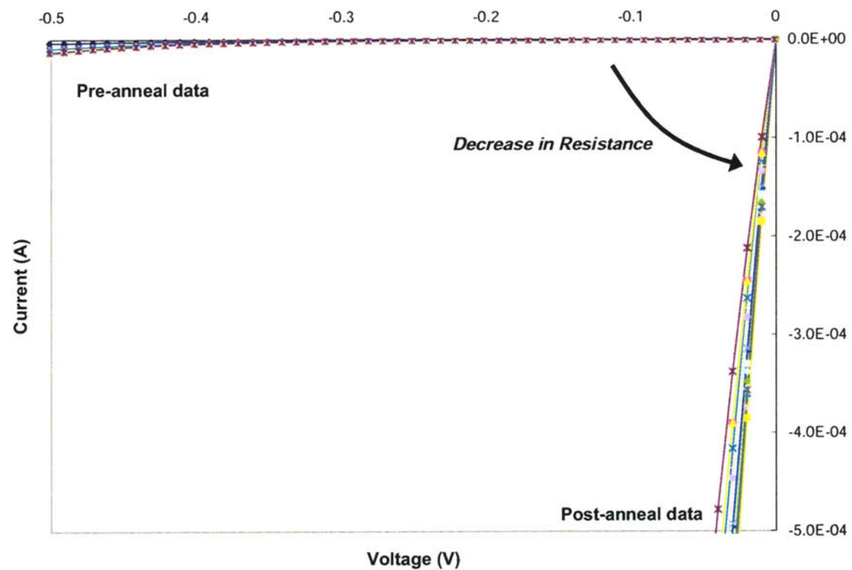

Temperature Effects

On a GaAs tunnel diode (with 0% Indium), measurements were taken at room temperature on 90 μm contacts. Measurements on the same contacts were then repeated after cooling the wafer 6°C colder with Falcon Dust-Off, a Freon source. Figure 2.27 demonstrates the effect of a change in temperature on the tunneling behavior of a device. Reducing the free carrier concentration by decreasing the temperature decreases the amount of tunneled current for a given applied bias. Thus, the resistance is increased.

FIGURE 2.27 Temperature effect on reverse-biased tunneling resistance.

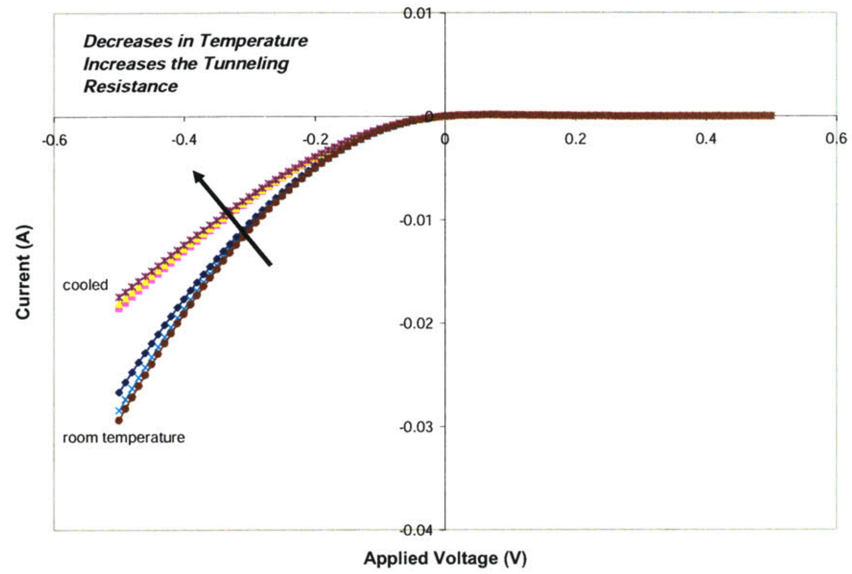

3.0 QUANTUM DOT AND QUANTUM DASH LASERS

3.1 Background and Design Theory

3.1.1 Semiconductor Lasers

There are three main types of interactions between electrons and photons in a material: spontaneous emission, stimulated absorption, and stimulated emission. All of which are depicted in Figure 3.1.

FIGURE 3.1 Three types of electron-photon interaction.

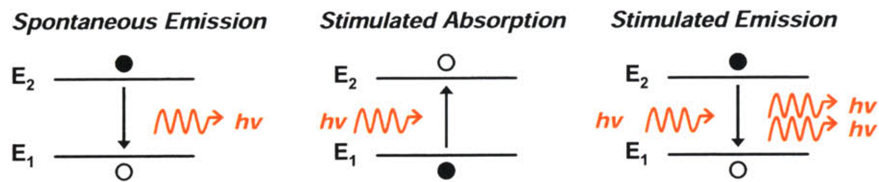

Spontaneous emission occurs when a higher energy electron recombines and falls from a high energy level to an unoccupied lower energy level, releasing its energy in the form of a photon. The energy loss in the process is given by:

$$E_g = E_2 - E_1 = hv = \frac{hc}{\lambda} \quad \text{(EQ 3.1)}$$

where h is Plank's constant, c is the speed of light, and v and λ are the frequency and wavelength, respectively, of the photon emitted.

On the other hand, stimulated absorption uses the energy of an incident photon to excite an electron from one energy level to a higher energy level. Light emitting diodes (LEDs) work by spontaneous emission; photodiodes are based on stimulated absorption.

Lasers operate by stimulated emission. When a photon with energy hv is incident upon an electron in a higher energy level, the electron falls to a lower energy level and releases a second photon of the same energy hv. This photon has the same frequency and phase as the initial photon. With continued stimulated emission in a material, photon amplification occurs, and monochromatic and coherent light is generated.

Furthermore, creating a laser requires both optical feedback and gain. Optical feedback helps maintain stimulated emission. By confining the photons in a laser cavity, photons can continue to stimulate the emission of more photons. As shown in Figure 3.2, a Fabry-

Perot cavity provides optical feedback by lining the edges of the cavity with reflective facets such that only standing waves are propagated.

FIGURE 3.2 Fabry-Perot cavity and modes.

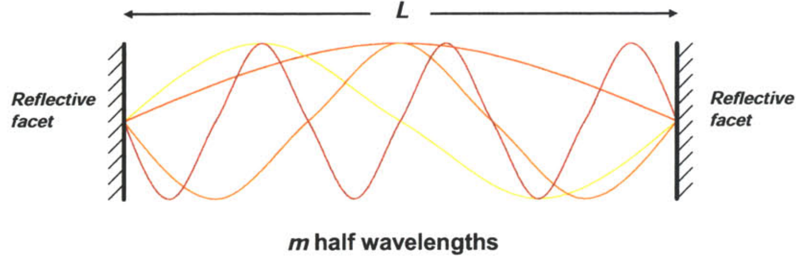

Thus, the use of reflective surfaces forms a standing wave pattern dependent on the length of the cavity. Only certain modes exist, given by:

$$\lambda_m = \frac{2L}{m} \quad \textbf{(EQ 3.2)}$$

where L is the length of the cavity, λ_m are the wavelengths supported, and m is an integer.

Besides some form of optical feedback, optical gain is also required. Thus, population inversion in the material must initially occur so that stimulated emission is more likely than internal absorption, yielding optical gain. A high concentration of electrons in the conduction band and holes in the valence band would allow recombination and photon emission to occur when a photon with the bandgap energy is incident on the device. Driving a p-n junction with a voltage greater than the bandgap can flood the conduction band with electrons and cause population inversion. Eventually, as the forward bias is further increased, enough carriers will exist such that optical gain occurs in the device. The switch from loss to gain occurs at the transparency point, which is shown in Figure 3.3 and given by

$$g = G(I - I_t) = GI - \alpha_i \quad \textbf{(EQ 3.3)}$$

where g is the gain per unit length within the cavity, G is the gain slope, and I_t is the transparency current density, and α_i is the loss of photons per unit length due to absorption. At the transparency current density, the device has a carrier concentration density of n_0.

FIGURE 3.3 Optical gain and loss versus drive current density.

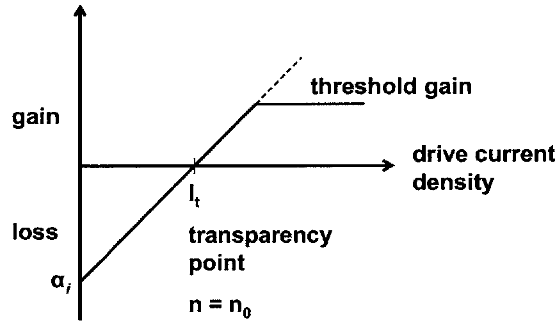

In a semiconductor laser, the rate equations are used to model the electrical and optical interaction within the device. The net carrier concentration in a laser per second is the sum of the rate of depletion of carriers through the generation of photons by spontaneous emission, the rate of increase of carrier concentration by current injection, and the rate of depletion of carriers through the generation of photons by stimulated emission. This is given below:

$$\begin{bmatrix}\text{Net change of carrier}\\ \text{contentration}\end{bmatrix} = -\begin{bmatrix}\text{Depletion of carriers through}\\ \text{spontaneous emission}\end{bmatrix} + \begin{bmatrix}\text{Rate of increase of carrier}\\ \text{concentration by current injection}\end{bmatrix} - \begin{bmatrix}\text{Depletion of carriers through}\\ \text{stimulated emission}\end{bmatrix}$$

$$\frac{dn}{dt} = -\frac{n}{\tau_s} + \frac{\eta_i I}{qV} - g(n - n_o)P \qquad \text{(EQ 3.4)}$$

Thus, spontaneous emission is dependent upon the carrier concentration in the laser, n, and the spontaneous recombination time of carriers, τ_S, where

$$\frac{1}{\tau_s} = \frac{1}{\tau_{rr}} + \frac{1}{\tau_{nr}} \qquad \text{(EQ 3.5)}$$

or the sum of the lifetimes associated with radiative, τ_{rr}, and non-radiative, τ_{nr}, recombination. The increase in carrier concentration is given by the injected laser current, I, the charge of an electron, q, and the volume of the active region, V. However, as in a light emitting diode, only a percentage of the electrons that recombine with holes actually generate a photon. The internal current injection efficiency, η_i, is the ratio of the number of photons generated to the number of electrons injected. The last term of Equation 3.4 models stimulated emission and is defined by the gain constant, g, the transparency carrier density, n_o, as depicted in Figure 3.3, and the photon density in the lasing mode, P.

When lasing begins, the net change of carrier concentration is zero, as all injected carriers are recombined to emit photons. Thus, the carrier concentration in the laser is constant, and $n = n_{th}$. Given this, the rate equation can be solved for the optical power generated by the laser:

$$P = \frac{\frac{\eta_i I}{qV} - \frac{n_{th}}{\tau_s}}{g(n_{th} - n_o)} = \eta_i \cdot \frac{I - I_{th}}{qV \cdot g(n_{th} - n_o)} = \eta_i \cdot k \cdot (I - I_{th}) \tag{EQ 3.6}$$

where

$$I_{th} = \frac{n_{th} qV}{\eta_i \tau_s} \tag{EQ 3.7}$$

Thus, above a certain threshold current, I_{th}, the optical power is proportional to the injected current. Below operation at the threshold current, the device behaves like a diode and the voltage varies exponentially with the drive current.

Figure 3.4 shows the relationship between the generated optical power for a given injected current. A linear relationship occurs after the threshold current is reached.

FIGURE 3.4 Relationship between the optical power generated for a given current injection.

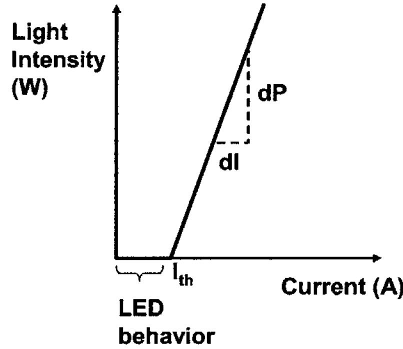

However, not all of the power generated by the photons is emitted by the laser. Losses in the mirrors contribute to the overall performance. In the cavity, the number of photons leaving per unit time is given by the loss per unit length in the active material, or

$$\alpha_m = \left(\frac{1}{2L}\right) \cdot \ln\left(\frac{1}{R_1 R_2}\right) \tag{EQ 3.8}$$

where R_1 and R_2 are the reflection coefficients of the mirrors. Thus, assuming the facets are the same ($R_1 = R_2$), the output power through one facet is given by

$$P_{out} = \frac{1}{2} \cdot \begin{bmatrix} \text{Photon} \\ \text{Energy} \end{bmatrix} \cdot \begin{bmatrix} \text{Total number} \\ \text{of photons} \end{bmatrix} \cdot \begin{bmatrix} \text{Proportion of photons leaving} \\ \text{the cavity per second} \end{bmatrix}$$

$$P_{out} = \frac{1}{2} \cdot hv \cdot [PV] \cdot \left[v_g \cdot \left(\frac{1}{2L}\right) \cdot \ln\left(\frac{1}{R_1 R_2}\right) \right]$$

$$P_{out} = \frac{hvPVv_g \ln \frac{1}{R_1 R_2}}{4L} \qquad \text{(EQ 3.9)}$$

where hv is the energy of the photon, P is the density of photons in the cavity, V is the volume of the cavity, and v_g is the speed of light in the laser cavity. The differential efficiency is therefore proportional to the photons leaving the cavity over the total number of photons, or

$$\eta_D = \eta_i \cdot \frac{\text{loss due to photons leaving the cavity}}{\text{total loss}} = \eta_i \cdot \frac{\alpha_m}{\alpha_i + \alpha_m} \qquad \text{(EQ 3.10)}$$

where η_i is the internal injection current efficiency, α_m is the loss per unit length in the cavity due to photon transmission through facets, as defined in Equation 3.8, and α_i is the loss per unit length due to scattering and absorption in the material, as defined in Equation 3.3. Thus, the external differential efficiency can also be the ratio of output power to input power or the ratio of output current to input current. Consequently, the output power can be given as follows:

$$P_{out} = \eta_D \cdot \frac{hv}{q} \cdot (I - I_{th}) \qquad \text{(EQ 3.11)}$$

The external differential efficiency is therefore proportional to the ratio of the power output to the current injected into the laser.

Similar to LEDs, lasers are affected by changes in temperature. At higher temperatures, spontaneous emission is more likely to occur and a higher current is needed to maintain population inversion for lasing. The threshold current density's dependency on temperature is given by

$$J_{th} = J_0 \exp\left(\frac{T}{T_0}\right) \qquad \text{(EQ 3.12)}$$

where T_0 is typically 150 K for a GaAs laser. Figure 3.5 demonstrates the shift in lasing for an increase in temperature. For small changes in temperature, the differential efficiency is assumed to be constant.

FIGURE 3.5 The effect of temperature on optical power output and threshold current.

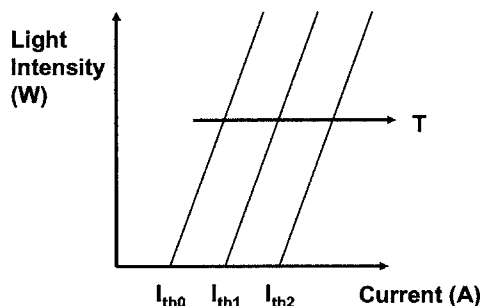

Thus, increasing the temperature can effectively turn a laser off if the threshold current is no longer reached. Additionally, saturation in the output power occurs at high temperatures or drive levels. The sub-linear performance is caused by current leakage across the junction and by Auger or nonradiative recombination, where the recombination energy of an electron is passed to another electron instead of photon emission.

3.1.2 Laser Structures

In a p-n junction laser, two opposite sides of a junction are cleaved or polished; whereas, the other two sides are roughened to prevent lasing in that direction. For this structure, the current density is very sensitive to temperature. For example, a GaAs p-n junction laser has a threshold current density at room temperature of approximately 5×10^4 A/cm^2, which makes continuous operation difficult.

A double heterostructure can reduce the current density sensitivity to temperature by sandwiching the active region with materials of a lower refractive index and a higher bandgap. The sharp reduction in the refractive index confines the optical field, and the higher potential barriers provide carrier confinement. Many more complex heterostructures exist that can provide carrier and optical confinement, and the reader is directed to [8] for a more detailed explanation.

Quantum wells can further improve the behavior of a laser. Instead of using bulk material, quantum wells exploit quantization by setting the thickness of the active layer to roughly the carrier de-Broglie wavelength, given by $\lambda = h/p$, where h is Planck's constant and p is the momentum. The result is a discrete density of states so that recombination occurs between well-defined energy levels instead of between the parabolic spread in energy levels found in bulk semiconductor. The size of the quantum well determines the number and

separation of energy levels in the quantum well and, therefore, the wavelength of the light emitted.

3.1.3 Tunnel-Junction-Coupled Lasers

As previously mentioned, an inherent limit to the injection current efficiency exists for a single stage laser: an electron can stimulate the emission of at most one photon. However, epitaxially coupling two lasers with a tunnel junction diode allows an electron to recombine in the first active layer and then tunnel into and recombine in the second active layer. Figure 3.6 depicts a tunnel-junction-coupled laser and demonstrates how two photons can be emitted by a single electron.

FIGURE 3.6 Tunnel-junction-coupled laser depicting how electron tunneling can stimulate emission in two lasers.

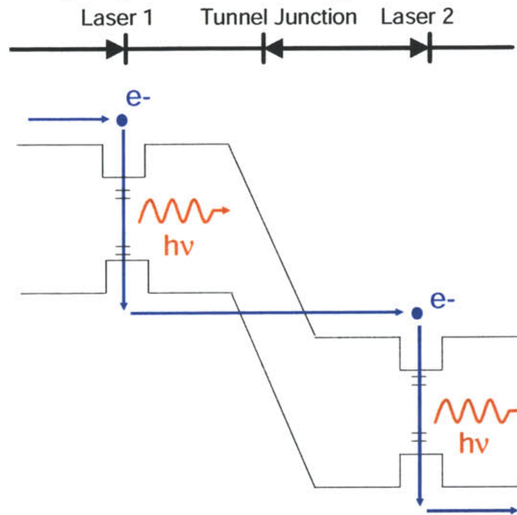

Since the cascaded lasers are essentially connected in series, the voltage drop and external quantum efficiency of the device are simply the sum of the parameters for the individual lasers. As in a single stage laser, the output power is given by Equation 3.11. However, the differential efficiency is now given by

$$\eta_D = N \cdot \eta_i \cdot \frac{\alpha_m}{\alpha_i + \alpha_m} = \sum_{k=1}^{N} \eta_{ik} \cdot \frac{\alpha_m}{\alpha_i + \alpha_m} \quad \text{(EQ 3.13)}$$

where N is the number of cascaded lasers, η_{ik} is the injection efficiency of each stage cascaded, and α_m and α_i are the loss from facets and internal absorption, respectively. In practice, the tunnel junction diodes themselves incur an additional optical loss, and the external efficiency therefore does not scale completely to the number of lasers.

Ideally, the threshold current is independent of the number of stages. However, in a tunnel-junction-coupled laser, the tunnel junctions introduce a slight loss in gain. Additionally, depending on the exact structure of the laser, the current may spread laterally as it moves through the device, such that the active region volume is smaller at the top than it is in the bottom gain section. Consequently, the second stage has a higher threshold current, resulting in a discontinuity in the output power-current behavior due to the two threshold currents.

Esaki first introduced the semiconductor tunnel junction in 1974 [4]. Since then, tunnel-junction-coupled lasers have been successfully fabricated. Vertical cavity surface emitting lasers have been demonstrated [9] [10], and edge emitting lasers have also been demonstrated under pulsed operation [11] [12]. Room temperature, continuous-wave operation of a tunnel-junction-coupled laser was also achieved. [13] Be and Si were used to heavily dope GaAs to form the tunnel junction between two epitaxially-stacked lasers. An external quantum efficiency of 99.3% was reported for a 990 nm wavelength emission.

3.1.4 Quantum Dots

Quantum wells have been previously used to improve the flexibility of wavelength emission in lasers, but GaAs-based quantum well lasers are still constrained to the red and near-infrared region. Because of material constraints, strained quantum wells of $In_xGa_{1-x}As$ emit light with a maximum wavelength of roughly 1100 nm. Fortunately, the introduction of InAs quantum dots (QD) increases the wavelength emission range to ~1300 nm. Additionally, nonradiative recombination is significantly reduced as the spread in density of states is reduced with quantum dots. Figure 3.7 shows the density of states as a function of energy for a bulk semiconductor, a quantum well, and uniform quantum dots.

FIGURE 3.7 Density of states diagram for bulk, quantum well, and quantum dot structures.

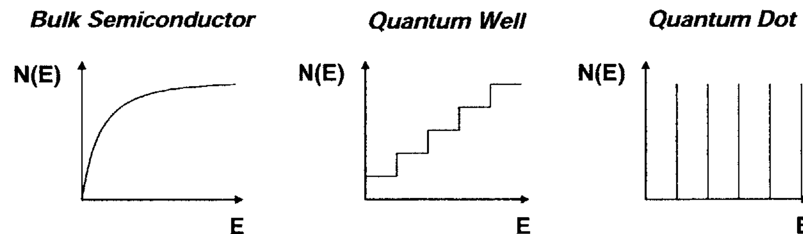

Quantum dots are formed by purposely depositing lattice-mismatched material onto the substrate material, resulting in small islands of active material on the substrate. So, although InAs and GaAs do not have matching lattice constants, they are nevertheless epitaxially compatible. The Stranski-Krastanov model predicts the resulting island formation, and the critical thickness set by the Matthews-Blakeslee condition is not applicable. Thus, while the band structure of the device can be altered by means of quantum dot incorpora-

tion, dislocations are avoided and the laser does not suffer from excessive nonradiative recombination.

Molecular Beam Epitaxy (MBE) can be used to produce quantum dots on the substrate. Precise control of growth conditions like substrate temperature, deposition rate, and As flux permits control of the dot size and dot density and therefore the emission wavelength and intensity.

GaAs-based quantum-dot lasers have been shown to successfully emit 1300 nm wavelength at room-temperature. [14] [15] [16] Along with near-infrared emission, both improved gain and increased temperature stability were also demonstrated. In [17], a very low $16 A/cm^2$ threshold current density was achieved by implementing a single dots-in-a-well (DWELL) structure. The quantum well structure was found to help quantum dots capture carriers and thus greatly improve the internal quantum efficiency of the device.

3.1.5 Quantum Dashes

InAs quantum dots on GaAs wafers are limited to emission at ~1300 nm. To extend the range of emission wavelength, InAs quantum dot structures have been grown on InP [18] [19], resulting in quantum dash structures. When the InAs 'dots' are grown in an InGaAsP quantum well on an InP substrate, the 'dots' are elongated into dashes along the [011] axis due to the directional favor in mobility. However, on AlGaInAs layers on InP substrates, InAs quantum dots can be formed.

For an InAs quantum dash laser, [18] reported emission wavelengths from quantum dash lasers on InP between 1.6 to 1.66 μm at room temperature with a low threshold current density. Schwertberger et. al. [19] reported emission from 1.54 to 1.78 μm though both threshold current densities and operation temperatures were higher. Nonetheless, these higher wavelengths have applications in long-distance optical networks and sensor applications.

3.1.6 Design of Quantum Dot Lasers

Quantum dot lasers were designed for 1300 nm emission. Additionally, as aforementioned, tunnel diodes can be used to epitaxially connect two lasers to create a tunnel-junction-coupled laser. Therefore, the efficiency of a quantum-dot laser can be improved if coupled with a tunnel junction. The quantum-dot lasers fabricated in the lab were thus cascaded and connected by a highly reversed-biased p-n junction diode to create tunnel junction quantum dot lasers. The two stages were connected via an InGaAs tunnel junction.

The InAs quantum dots were placed in an InGaAs quantum well to encourage carrier confinement. Three dots-in-a-well (DWELL) structures were made with 6 nm $In_{0.15}Ga_{0.85}As$ quantum wells and 25 nm GaAs spacers. This core region was grown at a substrate temperature of 500°C to optimize the emission wavelength and intensity given by the quantum dots. As a cladding layer, $In_{0.51}Ga_{0.49}P$ was used as it is lattice-matched to GaAs and

is grown at a temperature of 480°C which prevents material mixing in the quantum dot area. The cladding layers were doped with Si and Be at a concentration of 10^{18} cm^{-3}.

For the tunnel-junction-coupled laser, a tunnel junction layer was grown at 480°C before another quantum dot laser was grown. Both the single stage and two stage laser were capped with highly doped GaAs. Figure 3.8 shows the device structure of the single stage quantum dot laser and the quantum dot tunnel-junction-coupled laser.

FIGURE 3.8 Device structure of the quantum dot lasers.

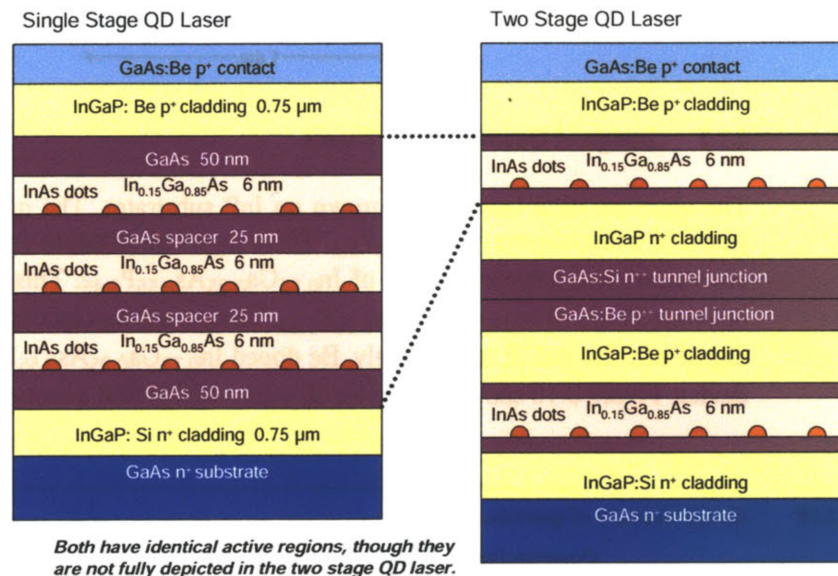

The InAs quantum dot lasers were grown on a GaAs-based substrate. As shown in Figure 3.9, atomic force microscopy confirms the existence of quantum dots, with an average diameter of 23 nm with a density of 4.2×10^{10} cm^{-2}. Photoluminesence also confirmed 1300 nm wavelength emission from a single stage fabricated quantum-dot laser.

FIGURE 3.9 Atomic force microscopy of gas source molecular beam epitaxially-grown InAs quantum dots [6]

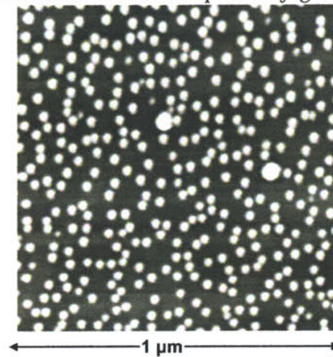

3.1.7 Design of Quantum Dash Lasers

The quantum dash lasers were grown on InP substrates. The quantum dashes are composed of 4 monolayers of $InAs_{0.9}P_{0.1}$. Three layers of quantum dashes are grown and each are sandwiched between 30 nm of $In_{0.75}Ga_{0.25}As_{0.55}P_{0.45}$. This stack is then embedded between 50 nm of $In_{0.82}Ga_{0.18}As_{0.36}P_{0.64}$. The p+ and n+ cladding layers consisted of InP doped with Be and Si, respectively. Be doped $In_{0.75}Ga_{0.25}As_{0.55}P_{0.45}$ was used to cap the device. Figure 3.10 shows the device structure of this first quantum dash laser design (I).

FIGURE 3.10 Device structure of quantum dash laser.

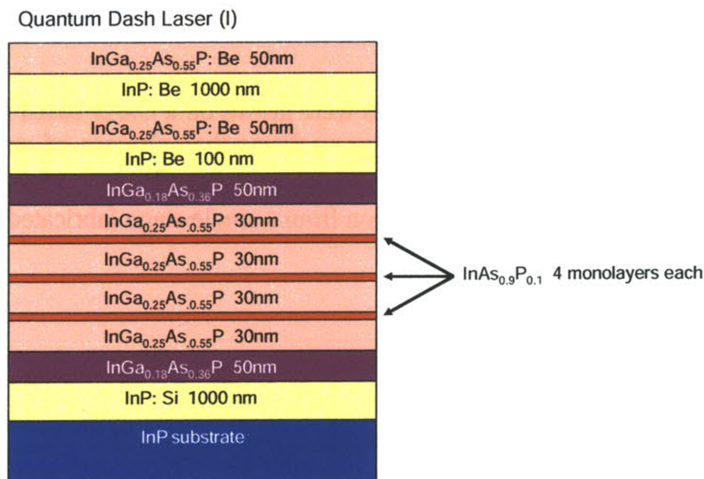

A second growth (II) of a similar structure was performed. However, the p+ and n+ InP layers had a doping gradient, and the thickness of the $In_{0.82}Ga_{0.18}As_{0.36}P_{0.64}$ layers were

60 nm. Figure 3.11 shows a scanning electron micrograph (SEM) of the MBE-grown $InAs_{0.9}P_{0.1}$ quantum dashes. The 1 μm by 1 μm cross section has an average peak-to-peak roughness on the order of about 3 nm.

FIGURE 3.11 Scanning electron micrograph (SEM) of the $InAs_{0.9}P_{0.1}$ quantum dashes grown using MBE.

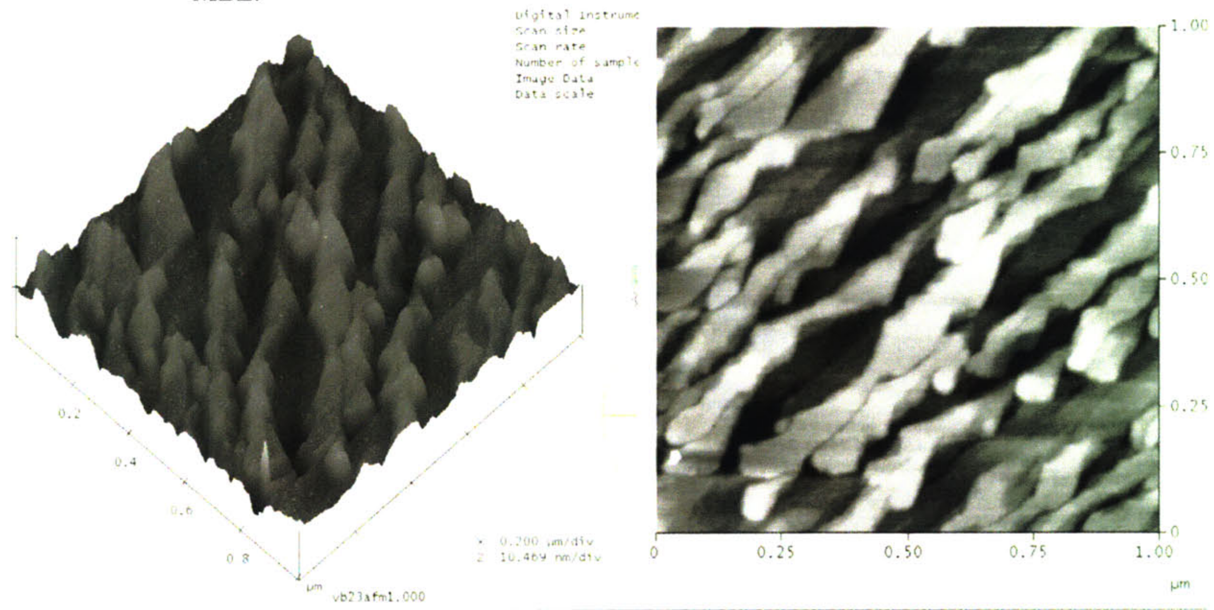

3.1.8 Laser Fabrication

Both the quantum dot and quantum dash lasers were fabricated into oxide stripe lasers. The fabrication process is outlined below:

- Deposition of 250 nm of hydrogensilsesquioxane (HSQ) as an insulator
- Cure HSQ in N_2 at 400°C for 1 hour
- Photolithography to pattern stripes 5 to 50 μm wide
- H_2O:HF (10:1) etch
- Photolithography of metal contacts
- Deposition of Ti/Pt/Au
- Metal lift-off
- Backside polish with alumina to a substrate thickness of 150-200 μm
- Backside metal deposition
- Rapid thermal anneal

The backside metal layer on the GaAs substrate of the quantum dot lasers consisted of Ti/Pt/Au (300/200/2000Å). Layers of Ni/Au/Ge/Au/Ni/Au (50/100/500/900/300/2000Å) were deposited on the backside of the InP-substrate quantum dash devices. [6]

Figure 3.12 shows the fabrication results of the quantum dash lasers. The quantum dot lasers showed identical results.

FIGURE 3.12 Nomarski micrograph of the quantum dash laser (II).

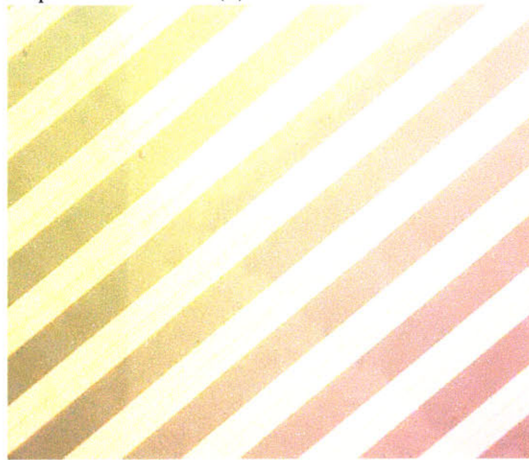

3.2 Research Approach

3.2.1 Research Objective

The goal is to electrically characterize single stage quantum dot lasers, quantum dot tunnel-junction-coupled lasers, and quantum dash lasers. The InAs-InGaAs-GaAs quantum dot lasers are designed to emit at 1300 nm. Successful growth and fabrication will enable the lasing efficiency and threshold current of these devices at room temperature to be analyzed. Additionally, the two stage lasers should exhibit similar trends of a tunnel-junction-coupled laser: an increase in efficiency, an increase in voltage drop, and a constant threshold.

The quantum dash laser devices will be tested to measure the emission wavelength and optical output characteristics of the devices under continuous and pulsed operation.

3.2.2 Laser Mounting Design

Testing of the quantum dot and quantum dash devices are only possible with effective mounting of the lasers. Two packaging methods are analyzed: the first involves Cu mounts; the second involves CuW mounts.

The Cu mounts are approximately 0.5 mm thick and cut in the MIT machine shop; Figure 3.13 shows the dimensions of the mounts. The dimensions are selected to mirror the dimensions of a sample holder typically implemented in a fiber coupling setup.

FIGURE 3.13 Dimensions of copper mounts.

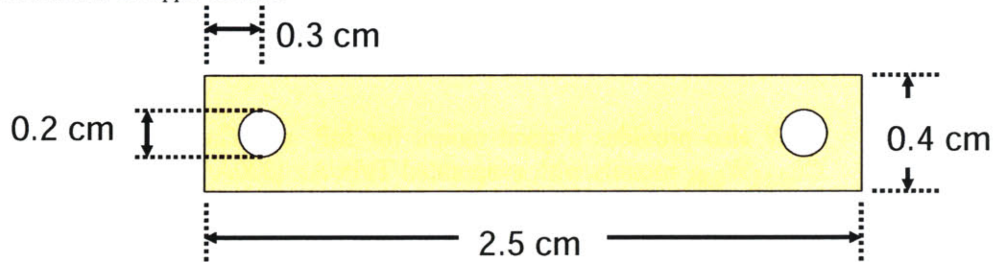

Once the Cu surface is cleaned thoroughly, Ti/Pt/Au (500Å/1000Å/300Å) is deposited, followed by a 2 µm thick layer of sputtered Indium. The Au layer is kept thin to avoid interaction with the solder alloy.

Before the device is mounted, the layer of Indium is lightly scrubbed with a Fluorine-based flux to not only remove the native In-oxide layer but to also prevent further oxidation. To remove the flux, the mount is then rinsed with water and methanol, and then dried.

The substrate, with metal already deposited on the backside as previously discussed in Section 3.1.8, is positioned on the mount and is heated on a Carbon strip in an N_2-filled bell jar. Slight pressure via a probe is applied to the device. If more than one device is mounted, a ceramic strip is used to disperse the pressure across the various devices evenly. The contents of the jar are heated to at least a temperature of 156°C to melt the layer of Indium. Once the Indium melts, the heat and pressure are turned off.

Figure 3.14 summarizes the process by depicting the final mounted device structure. The metallization was performed in the Nanostructures Laboratory; the mounting process was performed at MIT Lincoln Laboratory with the guidance of Leo Missaggia.

FIGURE 3.14 Structure of metals used to solder the GaAs or InP device to a copper mount.

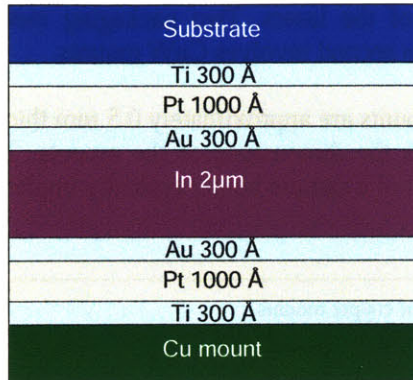

CuW also provides a good mount for InP- and GaAs- based devices. Pre-fabricated $Cu_{0.15}W_{0.85}$ mounts with evaporated Ti/Pt/Au (300Å/200Å/2000Å) and a 2 µm layer of evaporated $Au_{0.10}Sn_{0.90}$ solder are used. The CuW mounts have similar dimensions to the Cu mounts as depicted in Figure 3.13. While $Au_{0.80}Sn_{0.20}$ is commonly used in industry to ensure long-term reliability, $Au_{0.10}Sn_{0.90}$ is easier to use with its lower melting point and still minimizes surface oxidation.

Before the substrates are soldered, the metallized CuW mounts are sputtered in an Argon plasma for 10 minutes using Reactive Ion Etching (RIE). This step removes any oxide from the AuSn surface.

The various GaAs and InP devices, with their respective back-side metals, are immediately placed on the cleaned mounts. They are annealed on a carbon strip in an N_2-filled bell jar by heating the structure to just above the 217°C melting point. Similar to the Cu mounting procedure, a small pressure is applied directly to the device during the heating to insure that a satisfactory contact is created.

Figure 3.15 shows the final mounted device structure, depicting the metals used for the CuW mount. All of the steps of the mounting process are performed at MIT Lincoln Laboratory.

FIGURE 3.15 Structure of metals used to solder the GaAs and InP devices to a CuW mount.

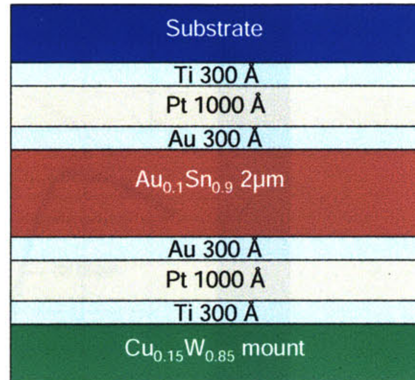

3.2.3 Electrical Testing Design

The quantum dot devices are tested under continuous operation, and Figure 3.16 shows a block diagram of the setup. A laser diode driver feeds current through a probe, and an optical multimeter reads the optical output power through an InGaAs photodetector.

FIGURE 3.16 Diagram of continuous operation testing using an InGaAs photodetector.

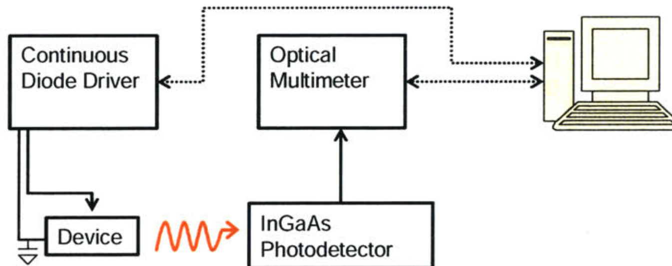

The InGaAs photodetector is only sensitive up to 1600 nm. As the wavelength emission of the quantum dash lasers are unknown, a PbS detector will be used to test the InP devices if the emission is above the InGaAs photodetector range. As shown in Figure 3.17, PbS photocells have good sensitivity up to ~2.5 μm. Figure 3.18 shows the schematic of the testing setup. Both the pulsed diode driver and the PbS detector feed into a lock-in amplifier. The output of the lock-in amplifier will be collected and analyzed by a Labview program.

FIGURE 3.17 Wavelength detection range of an PbS detector [20]

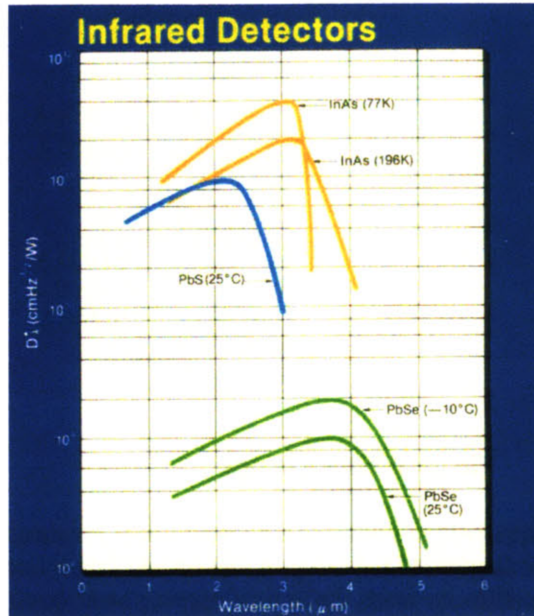

FIGURE 3.18 Diagram of continuous or pulsed operation testing using an PbS photodetector.

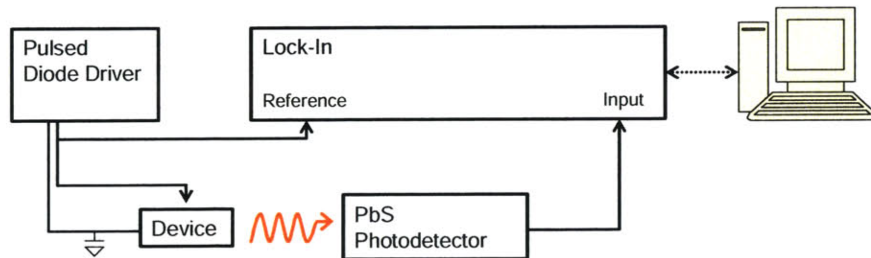

Figure 3.19 shows the circuit diagram of the PbS detector that was built. The goal of the PbS detector design is to provide a regulated DC power source and to adjustably amplify the detected signal. Table 4 lists the values of the resistors and capacitors used in the circuit.

FIGURE 3.19 Schematic of PbS detector circuit.

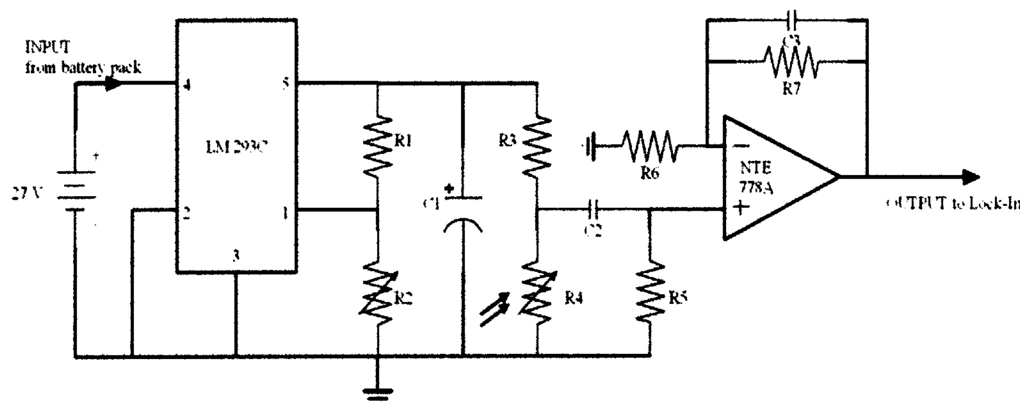

Three 9 V batteries are used to power the circuit via an LM 293C voltage regulator. The voltage divider set by R1 and the potentiometer R2 provides a voltage swing between 1.67 V and 27 V. R4 is the PbS photocell and acts as a variable resistor. Thus, when the device is driven by a pulsed input source, R1 and R2 ultimately set the amplification of the signal. On the other hand, power amplification of the signal is provided by the NTE 778A op-amp and surrounding circuit. For equal values of R6 and R7, a theoretical gain of 2 is provided. Band pass filtering between 77.3 Hz and 9.9 kHz is provided by the R5C2 and R7C3 configurations.

A slight modification was made to the final circuit to avoid reaching the voltage limit of the op-amp as determined by the +/- 9 V supply voltage. The positive input (+) to the op-amp is biased at zero volts: instead of being connected directly to ground, R5 is connected to the + 9 V supply and another resistor of equal value to R5 is connected to the - 9 V supply as well as the positive (+) input to the op-amp. This also improves the bandwidth range to 99.3 Hz and 9.9 kHz. The circuit is packaged in an Aluminum box and implemented in the setup depicted in Figure 3.18.

TABLE 4. Impedance values for the PbS detector circuit.

Device	Value
R1	4.7 kΩ
R2	75 Ω – 100 kΩ
R3	1 MΩ
R4	660 kΩ (off) or 1.75 MΩ (on)

TABLE 4. Impedance values for the PbS detector circuit.

Device	Value
R5	330 kΩ
R6	330 kΩ
R7	330 kΩ
C1	470 μF
C2	0.002 μF
C3	100 pF

3.3 Results and Discussion

3.3.1 Packaging

Photoluminesence was performed on the as-grown quantum dot wafers. As Figure 3.20 shows, the photoluminesence emission was observed at 1350 nm. The lasers were then fabricated into oxide stripe lasers, as detailed in Section 3.1.8. The single-stage and two-stage devices were cleaved to form cavity lengths of 930 μm and 1002 μm, respectively. The quantum dash lasers were cleaved into 540 μm (I) and 745 μm (II) long cavities.

FIGURE 3.20 Room temperature photoluminesence of quantum dot laser epilayer [20]

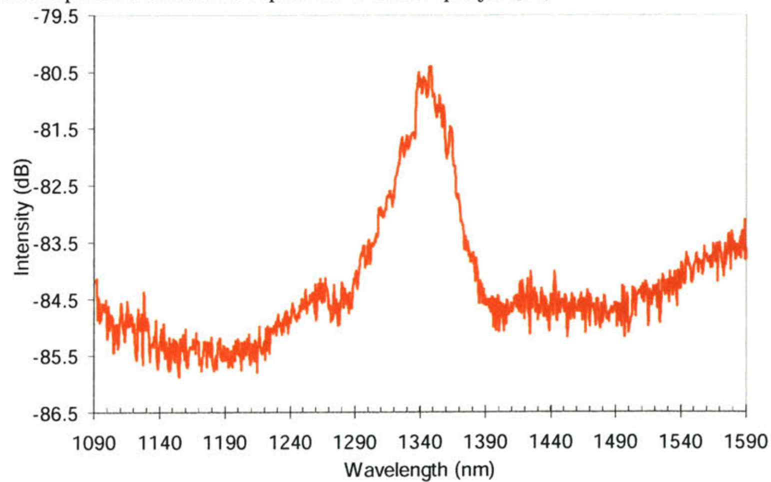

The cleaved devices were then mounted on the Cu and CuW mounts as outlined in Section 3.2.2. Both mounting designs were successful such that the devices exhibited negligible resistance though the mounts (the In/Au/Pt/Ti/Cu or AuSn/Au/Pt/Ti/CuW layers).

However, the CuW mounting procedures proved to be more successful as sections of the metal layer stack did not adhere well to the Cu mount and peeled off during the N_2 ambient heating, revealing the Cu mount below. This was most likely a result of inadequate cleaning of the manufactured Cu mount. With a more intense pre-etch of the Cu mount before sputtering, the mounting design can be successfully implemented in future GaAs applications.

3.3.2 Quantum Dots

Using the setup depicted in Figure 3.16, a DC current source was used to test the single-stage and two-stage quantum dot lasers. Figure 3.21 shows the voltage-current behavior of the quantum dot lasers. The current is normalized to the area of the active region. The results demonstrate a threshold voltage at which the devices turn on. As previously discussed, this bias provides the necessary population inversion for lasing to begin to occur.

FIGURE 3.21 Voltage characteristics of a single stage and two stage laser.

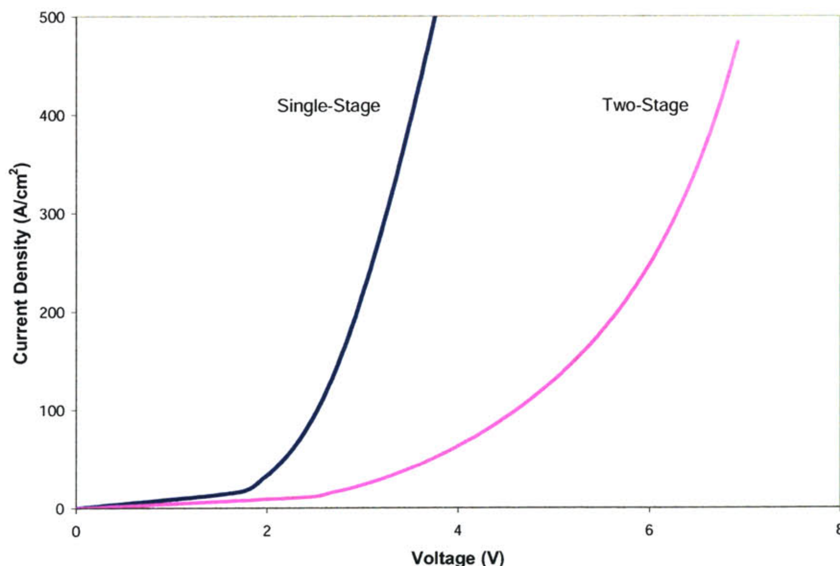

More importantly, Figure 3.21 also depicts an increase in the threshold voltage for the tunnel-junction-coupled two-stage laser as compared to the single-stage laser. In a tunnel-junction-coupled laser, the voltage drop across the device should scale linearly with the number of epitaxially-stacked lasers. Figure 3.21 shows that the voltage drop across the two-stage laser is slightly more than double that of the single-stage laser. The additional voltage drop is most likely due to the voltage across the tunnel junction used to couple the cascaded lasers.

The optical output power is plotted versus the current density as shown in Figure 3.22. For a given current bias, the light intensity from a two-stage laser is dramatically greater than a single-stage laser. Electrons can stimulate emission in two active regions by tunneling through a tunnel junction in a cascaded laser. The external quantum efficiency, normalized by area (W*cm^2/A), is 3.32 times greater in a two-stage laser than for a single stage laser. The fact that the efficiency gain is more than doubled can be attributed to potentially lower contact resistance or lower loss within the two-stage laser. The threshold current, area, threshold current density, and the external quantum efficiency for a 26.1 x 930 μm single-stage laser and a 26.7 x 1002 μm two-stage laser is listed in Table 5.

FIGURE 3.22 Output power for a single and two-stage laser.

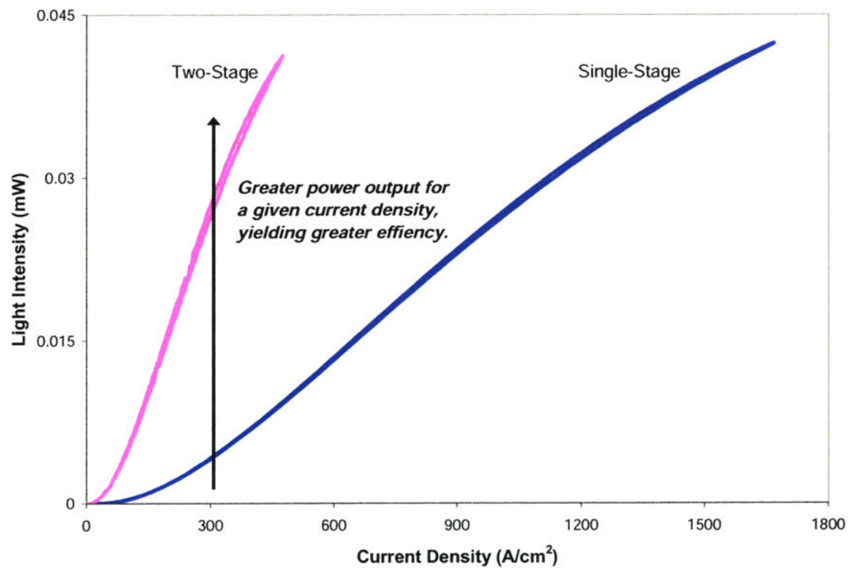

TABLE 5. Lasing parameters of a 26.1 x 930 μm single-stage laser and a 26.7 x 1002 μm two-stage laser.

	Single-Stage	*Two-Stage*
Threshold Current (mA)	7.8	11.3
Area (cm^2)	4.8 x 10^{-5}	2.68 x 10^{-4}
Threshold Current Density (A/cm2)	163	42
External Quantum Efficiency (mW/A)	14.3%	42.9%

Also notable is the effect of heating on the devices. Figure 3.23 shows the output power behavior of a single-stage laser. The plot of the output light intensity consist of two lines

which indicate the upward ramping of the current to 3334 A/cm^2 followed by the downward ramping of the current to zero. The gap between the two optical power measurements indicates a loss in optical power when the current is being decreased, due to the heating that occurred when current is increased. With the device already on, the device is warmer during the period of downward ramping. And, as discussed in Section 3.1.1 and depicted in Figure 3.5, an increase in temperature increases the current necessary to achieve a given output power. On the other hand, the heating effects during ramping have a discernible effect on the voltage-current behavior of the device. Also, this phenomenon is not demonstrated in Figure 3.22 because the current there was ramped much more quickly (1 mA every 200 ms as opposed to 0.5 mA every 2000 ms). The total time the device was on was shorter, which prevented the device from heating during testing.

FIGURE 3.23 Heating effects on output behavior due to slow continuous operation.

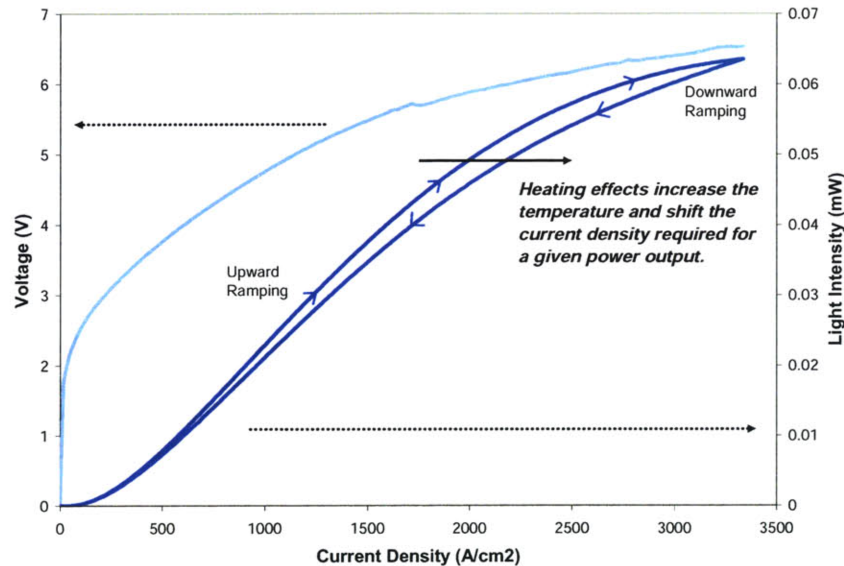

3.3.3 Quantum Dashes

Voltage-current characterization of the quantum dash devices demonstrated resistance values of approximately 1 kΩ. As a result, optical emission was not determined under continuous operation due to the voltage operating limit on the current source. Pulsed operation was not attempted due to the high resistance observed.

3.3.4 Future Work

Optical spectrum measurements of the quantum dot devices were desired, but light was unable to couple into the lensed fiber due to the low output powers. Attempts were made to drive the devices to higher output powers, but the maximum output power for the sin-

gle-stage and two-stage lasers were 54 μW and 45 μW, respectively, before either the current source reached its voltage limit of 7 V or the device failed.

The oxide stripe fabrication design also contributed to the low power output. As seen in Figure 3.24, this laser structure does not confine carriers laterally. As a result, the current spreads outside of the calculated active area. The current spreading not only heats up the device more rapidly, but it also increases the error involved in calculating the current density.

FIGURE 3.24 Structure of a stripe laser, demonstrating lateral current spreading.

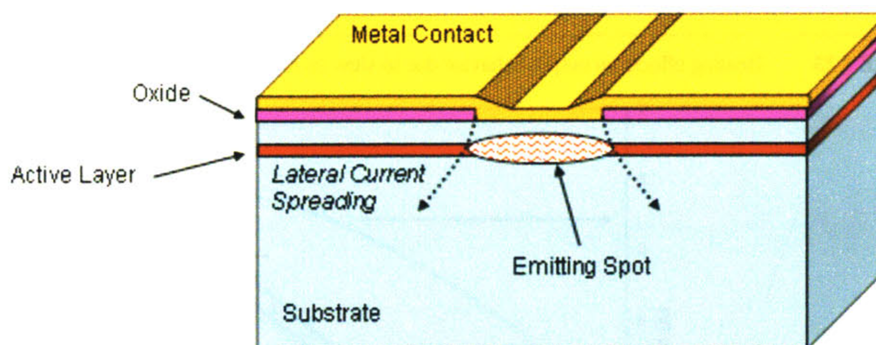

One possible solution to improve the optical output of the devices is to implement a more sophisticated laser structure that provides greater carrier confinement. Figure 3.25 shows an example of a ridge waveguide approach. The ridge above the active area minimizes current spreading. Reducing the amount of current needed for a given light output would reduce heating effects in the device.

FIGURE 3.25 Structure of a ridge laser with adequate lateral carrier confinement.

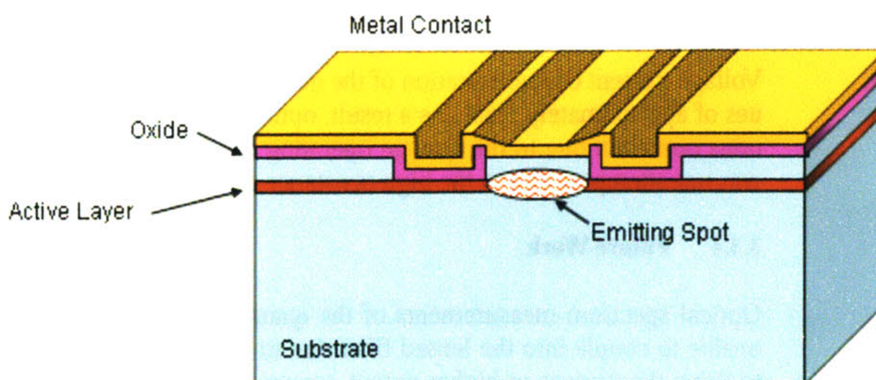

Another area of improvement would be to increase the length of the devices. For fixed facet loss, creating longer lasing cavities would not only increase the gain, but also provide more material to heatsink the device. As a result, lasing is further encouraged and the overall external quantum efficiency is enhanced.

4.0 SUMMARY

The goal of this work was to the characterize the behavior of tunnel-junction-coupled lasers as well as devices incorporating InAs quantum dots and quantum dashes to provide 1300 nm and 1550 nm wavelength emission, respectively, on III-V substrates.

The behavior of InGaAs tunnel junctions, that were implemented in tunnel-junction-coupled lasers, was initially analyzed. The InGaAs tunnel junction diodes have varying Indium contents ranging from 6.5% to 13.5% and the diameter of the diode mesas ranged from 3.5 μm to 90 μm. Variable angle spectroscopic ellipsometry was performed on the epi wafers to determine the InGaAs composition and epi layer thickness. Under both forward and reverse bias, the InGaAs tunnel junction diodes showed a very clear match to the electrical behavior predicted by theoretical modeling. First, the tunneling resistance decreased for increasing contact size. More importantly, the resistance decreased for increasing Indium content. In other words, not only does tunneling occur, but more electrons tunnel across the tunnel junction as the amount of Indium is increased due to the decrease of the InGaAs bandgap as the Indium content increases. Annealing the metal-semiconductor contact reduced the diode's overall resistance; reducing the diode's temperature increased the tunnel junction resistance.

With tunneling successfully demonstrated, the InGaAs tunnel junctions were implemented into two-stage lasers. Epitaxially connecting two lasers in series effectively doubles the external quantum efficiency of the overall device. Quantum dots grown on GaAs substrates were used in the active region of single-stage and two-stage devices. Photoluminescence confirmed the emission of the single-stage and two-stage quantum dot lasers; both emitted at ~1350 nm. As theoretically predicted, the tunnel-junction-coupled quantum dot lasers demonstrated higher efficiencies and higher turn-on voltages than single-stage quantum dot lasers. The increase in the threshold voltage in the two-stage laser was due to the drop across both lasers as well as the tunnel junction epitaxially connecting them. The higher output power was a result of the increase in photon emission by the tunneling of carriers between the two active regions. Unfortunately, lateral current spreading limited the output power of the quantum dot devices. Steps to improve carrier confinement in the devices should greatly increase the output optical power of the devices. Possible solutions include using a ridge waveguide or a buried ridge waveguide or lengthening the cavity of the device.

Two different mounting schemes were used to evaluate the GaAs-based quantum dot lasers and the InP-based quantum dash lasers. Although both schemes provided good electrical contact to the devices, the GaAs- and InP-based samples mounted with an AuSn-based metal stack adhered to its CuW mount better than the samples mounted with an In-based metal stack to its Cu mount.

Additionally, although InP-based quantum dash lasers were fabricated, no optical emission was observed due to the samples resistive nature. To insure that optical emission from

the devices could have been observed, a PbS photoconductor-based detector was constructed allowing an emission range up to 2.5 μm to be observed.

More broadly, this work provides a solid foundation for the development of exciting photonic devices. Quantum dots and quantum dashes provide novel ways of controlling wavelength emission. Furthermore, epitaxially coupling tunnel junctions can increase the external quantum efficiency of these devices.

5.0 REFERENCES

[1] Wikipidea. (n.d.). *Fiber to the Premises.* Retrieved April 20, 2006, from http://en.wikipedia.org/wiki/Fiber_to_the_premises

[2] Telecommunications Industry Association. (2006, April). *Fiber-to-the-Home Council and Telecommunications Industry Association Release Updated "U. S. Optical Fiber Communities" List.* (Publication No. JointPR06-03/04.26.06). Retrieved April 30, 2006, from TIA Online Press Releases: http://www.tiaonline.org/business/media/press_releases/2006/JointPR06-03.cfm

[3] E. F. Schubert, *Light Emitting Diodes* [Electronic version]. Cambridge University Press, 2003.

[4] L. Esaki, "Long Journey into Tunneling," *Proceedings of the IEEE,* vol. 62, no. 6, pp. 825-831, 1974.

[5] M. S. Tyagi, *Introduction to Semiconductor Materials and Devices.* New York: John Wiley & Sons, 1991.

[6] R. D. Williams, "Optical Logic and Quantum Dot Devices," Ph.D. Thesis, Department of Material Science and Engineering, Massachusetts Institute of Technology (forthcoming).

[7] S. Ahmed, M. R. Melloch, E. S. Harmon, D. T. McInturff, and J. M. Woodall, "Use of nonstoichiometry to form GaAs tunnel junctions," *Applied Physics Letters,* vol. 71, no. 25, pp. 3667-3669, 1997.

[8] L. A. Coldren and S. W. Corzine, *Diode Lasers and Photonic Integrated Circuits.* New York: John Wiley & Sons, 1995.

[9] W. Schmid, D. Wiedenmann, M. Grabherr, R. Jager, R. Michalzik, and K. J. Ebeling, "CW operation of a diode cascade InGaAs quantum well VCSEL," *Electronics Letters,* vol. 34, no. 6, pp. 553-555, 1998.

[10] T. Knodl, M. Golling, A. Straub, and K. J. Ebeling, "Multi-diode cascade VCSEL with 130% differential quantum efficiency at CW room temperature operation," *Electronic Letters,* vol. 37, no. 1, pp. 31-33, 2001.

[11] J. Ch. Garcia, E. Rosencher, Ph. Collot, N. Laurent, J. L. Guyaux, B. Vinter, and J. Nagle, "Epitaxially staked lasers with Esaki junctions: A bipolar cascade laser," *Applied Physics Letters,* vol. 71, no. 26, pp. 3752-3754, 1997.

[12] J. K. Kim, E. Hall, O Sjolund, and L. A. Coldren, "Epitaxially-stacked multiple-active-region 1.55 μm lasers for increased differential efficiency," *Applied Physics Letters,* vol. 74, no. 22, pp. 3251-3253, 1999.

[13] S. G. Patterson, E. K. Lau, K. P. Pipe, and R. J. Ram, "Temperature characteristics of bipolar cascade lasers," *Applied Physics Letters,* vol. 77, no. 2, pp. 172-174, 2000.

[14] D. L. Huffaker, G. Park, Z. Zou, O. B. Shchekin, and D. G. Deppe, "1.3 μm room-temperature GaAs-based quantum-dot laser," *Applied Physics Letters,* vol. 73, no. 18, pp. 2564-2566, 1998.

[15] Yu. M. Shernyakov, et. al, "1.3 μm GaAs-based laser using quantum dots obtained by activated spinodal decomposition," *Electronic Letters*, vol. 35, no. 11, pp. 898-900, 1999.

[16] A. E. Zhukov, et. al., "Continuous-Wave Operation of Long-Wavelength Quantum-Dot Diode Laser on a GaAs Substrate," *IEEE Photonics Technology Letters*, vol. 11, no. 11, pp. 1345-1347, 1999.

[17] G. T. Liu, A. Stintz, H. Li, T.C. Newell, A. L. Gray, P. M. Varangis, K. J. Malloy, and L. F. Lester, "The Influence of Quantum-Well Composition on the Performance of Quantum Dot Lasers Using InAs/InGaAs Dots-in-a-Well (DWELL) Structures," *IEEE Journal of Quantum Electronics*, vol. 36, no. 11, pp. 1272-1279, 2000.

[18] R.H. Wang, A. Stintz, P. M. Varangis, T. C. Newell, H. Li, K. J. Malloy, and L. F. Lester, "Room-Temperature Operation of InAs Quantum-Dash Lasers on InP (001)," *IEEE Photonics Technology Letters*, vol. 13, no. 8, pp. 767-769, 2001.

[19] R. Schwertberger, D. Gold, J.P. Reithmaier, and A. Forchel, "Long-Wavelength InP-Based Quantum-Dash Lasers," *IEEE Photonics Technology Letters*, vol. 14, no. 6, pp. 735-737, 2002.

[20] Hamamatsu Photonics, 325-6, Sunayama-cho, Hamamatsu City, Shizuoka Pref., 430-8587, Japan.

[21] P. Bhattacharya, Ed., *Properties of Lattice-Matched and Strained Indium Gallium Arsenide*. London: INSPEC, 1993.

[22] Ioffe-Physico-Technical Institute. (2003). *Physical Properties of Semiconductors*. Retrieved April 10, 2006 from New Semiconductor Material Archive: http://www.ioffe.rssi.ru/SVA/NSM/Semicond/index.html

6.0 APPENDIX

6.1 SimWindows Simulations

SimWindows is a freely available semiconductor device simulation program. It handles one-dimensional simulations of Si, GaAs, and AlGaAs devices. The materials database was consequently adapted to incorporate Indium as a GaAs alloy. The program was then used to simulate the band structure and quasi-Fermi levels of InGaAs tunnel junction diodes of various Indium contents. The device file for a tunnel junction with 15% Indium is included in Section 6.1.1; the complete materials file is included in 6.1.2. [21] [22]

6.1.1 Device File

```
#Simulation for InGaAs tunnel diode

grid length=.40 points=25
grid length=.05 points=50
grid length=.05 points=40
grid length=.05 points=40
grid length=.05 points=50
grid length=.40 points=25

structure material=gaas length=0.475
structure material=gaas alloy=in length=0.05 conc=0.15
structure material=gaas length=0.475

doping length=.4500 Na=1e+19
doping length=.05 Na=1e+19
doping length=.05 Nd=1e+19
doping length=.4500 Nd=1e+19
```

6.1.2 Material Parameters File

```
# This file is the general material parameters file. This lets you define
# arbitrary materials with arbitrary names. This file must be contained in
# the same directory as the simwin.exe file. It is loaded as soon as the
# program starts.

Material=Si

# PURE SI

Alloy=Default

BAND_GAP Model=Band_gap terms=1.124,0,0,-4.73e-4,636
ELECTRON_AFFINITY Model=Band_gap terms=4.05,0,0,2.365e-4,636
STATIC_PERMITIVITY Value=11.7

REFRACTIVE_INDEX Value=3.44
```

```
ABSORPTION Segments=4
start_e=0.0 end_e=1.1 value=0.0
start_e=1.1 end_e=2.5 model=power_absorption terms=6e3,0,0,1.1,2
start_e=2.5 end_e=3.2 value=6e3*(E-1.1)^2+8e4*(E-2.5)^2
start_e=3.2 end_e=100 value=6e3*(E-1.1)^2+8e4*(E-2.5)^2+1.26e6*(E-3.2)^0.5

THERMAL_CONDUCTIVITY Value=1.412
DERIV_THERMAL_CONDUCT Value=0

ELECTRON_MOBILITY   model=mobility   terms=88,0,0,300,-0.57,7.4e8,0,0,-2.33,1.432e17,-
2.546
HOLE_MOBILITY model=mobility terms=54.3,0,0,300,-0.57,1.36e8,0,0,-2.23,2.671e17,-2.546

ELECTRON_DOS_MASS Value=1.08
HOLE_DOS_MASS Value=0.81
ELECTRON_COND_MASS Value=0.26
HOLE_COND_MASS Value=.386
ELECTRON_SHR_LIFETIME Value=1.e-7
HOLE_SHR_LIFETIME Value=1.e-7
ELECTRON_AUGER_COEFFICIENT Value=1.5e-31
QW_ELECTRON_AUGER_COEFFICIENT Value=0.0
HOLE_AUGER_COEFFICIENT Value=1.5e-31
QW_HOLE_AUGER_COEFFICIENT Value=0.0
RAD_RECOMB_CONST Value=1.5e-10
ELECTRON_ENERGY_LIFETIME Value=1.e-8
HOLE_ENERGY_LIFETIME Value=1.e-8
QW_RAD_RECOMB_CONST Value=0.0
ELECTRON_COLLISION_FACTOR Value=-0.5
HOLE_COLLISION_FACTOR Value=-0.5

# PARAMETERS OF GAAS

Material=GaAs

# NO ALLOY DEFAULT

Alloy=Default

BAND_GAP Model=Band_gap terms=1.424,0,0,-5.405e-4,204
ELECTRON_AFFINITY Model=Band_gap terms=4.07,0,0,2.702e-4,204
STATIC_PERMITIVITY Value=13.18

REFRACTIVE_INDEX Model=oscillator_refractive_index

ABSORPTION Segments=6
start_e=0 end_e=g value=0
start_e=g end_e=g+1 value=2.698e3+8.047e4*(e-g)-6.241e4*(e-g)^2+7.326e4*(e-g)^3
start_e=g+1 end_e=g+1.4 value=-3.218e6+9.060e6*(e-g)-8.428e6*(e-g)^2+2.681e6*(e-g)^3
start_e=g+1.4 end_e=g+1.9 value=-1.615e7+2.600e7*(e-g)-1.338e7*(e-g)^2+2.303e6*(e-g)^3
```

```
start_e=g+1.9 end_e=g+2.6 value=8.383e5+2.442e5*(e-g)-3.226e5*(e-g)^2+8.482e4*(e-g)^3
start_e=g+2.6 end_e=g+4.0 value=7.83e5

THERMAL_CONDUCTIVITY Model=Thermal_Conduct terms=549.356,1,0,0,-1.25
DERIV_THERMAL_CONDUCT Model=Thermal_Conduct terms=-686.695,1,0,0,-2.25
ELECTRON_MOBILITY Value=8000
HOLE_MOBILITY Value=370
ELECTRON_DOS_MASS Value=0.067
HOLE_DOS_MASS Value=0.62
ELECTRON_COND_MASS Value=0.067
HOLE_COND_MASS Value=.62
ELECTRON_SHR_LIFETIME Value=1e-8
HOLE_SHR_LIFETIME Value=1e-8
ELECTRON_AUGER_COEFFICIENT Value=1.5e-31
QW_ELECTRON_AUGER_COEFFICIENT Value=1.5e-19
HOLE_AUGER_COEFFICIENT Value=1.5e-31
QW_HOLE_AUGER_COEFFICIENT Value=1.5e-19
RAD_RECOMB_CONST Value=1.5e-10
ELECTRON_ENERGY_LIFETIME Value=1.e-12
HOLE_ENERGY_LIFETIME Value=1.e-12
QW_RAD_RECOMB_CONST Value=1.54e-4
ELECTRON_COLLISION_FACTOR Value=0.5
HOLE_COLLISION_FACTOR Value=0.5

# ALUMINUM ALLOY PARAMETERS IN GaAs

Alloy=Al

BAND_GAP Segments=2
Start_x=0.00 end_x=0.45 Model=Band_gap terms=1.424,1.247,0,-5.405e-4,204
Start_x=0.45 end_x=1.00 Model=Band_gap terms=1.9,0.125,0.143,-5.405e-4,204

ELECTRON_AFFINITY Segments=2
Start_x=0.0 end_x=0.45 Model=Band_gap terms=4.07,-0.7482,0,2.702e-4,204
Start_x=0.45 end_x=1.0 Model=Band_gap terms=3.594,0.3738,-0.143,2.702e-4,204

STATIC_PERMITIVITY Value=13.18,-3.12

REFRACTIVE_INDEX Model=oscillator_refractive_index

ABSORPTION Segments=6
start_e=0 end_e=g value=0
start_e=g end_e=g+1 value=2.698e3+8.047e4*(e-g)-6.241e4*(e-g)^2+7.326e4*(e-g)^3
start_e=g+1 end_e=g+1.4 value=-3.218e6+9.060e6*(e-g)-8.428e6*(e-g)^2+2.681e6*(e-g)^3
start_e=g+1.4 end_e=g+1.9 value=-1.615e7+2.600e7*(e-g)-1.338e7*(e-g)^2+2.303e6*(e-g)^3
start_e=g+1.9 end_e=g+2.6 value=8.383e5+2.442e5*(e-g)-3.226e5*(e-g)^2+8.482e4*(e-g)^3
start_e=g+2.6 end_e=g+4.0 value=7.83e5

THERMAL_CONDUCTIVITY Model=Thermal_Conduct terms=549.356,1,12.7,-13.22,-1.25
DERIV_THERMAL_CONDUCT Model=Thermal_Conduct terms=-686.695,1,12.7,-13.22,-2.25
```

```
ELECTRON_MOBILITY Segments=2
Start_x=0.0 end_x=0.45 Value=8000,-22000,10000
Start_x=0.45 end_x=1.0 Value=-255,1160,-720

HOLE_MOBILITY Value=370,-970,740

ELECTRON_DOS_MASS Segments=2
Start_x=0.0 end_x=0.45 Value=0.067,0.083
Start_x=0.45 end_x=1.0 Value=0.85,-0.14

HOLE_DOS_MASS Value=0.62,0.14

ELECTRON_COND_MASS Segments=2
Start_x=0.0 end_x=0.45 Value=0.067,0.083
Start_x=0.45 end_x=1.0 Value=0.32,-0.06

HOLE_COND_MASS Value=0.62,0.14

ELECTRON_SHR_LIFETIME Value=1e-8

HOLE_SHR_LIFETIME Value=1e-8

ELECTRON_AUGER_COEFFICIENT Value=1.5e-31
QW_ELECTRON_AUGER_COEFFICIENT Value=1.5e-19

HOLE_AUGER_COEFFICIENT Value=1.5e-31
QW_HOLE_AUGER_COEFFICIENT Value=1.5e-19

RAD_RECOMB_CONST Value=1.5e-10

ELECTRON_ENERGY_LIFETIME Value=1.e-12
HOLE_ENERGY_LIFETIME Value=1.e-12

QW_RAD_RECOMB_CONST Value=1.54e-4

ELECTRON_COLLISION_FACTOR Value=0.5
HOLE_COLLISION_FACTOR Value=0.5

# INDIUM ALLOY PARAMETERS IN GaAs

Material=GaAs
Alloy=In

BAND_GAP Segments=2
Start_x=0.00 end_x=0.45 Model=Band_gap terms=1.424,-1.11,0.45,0,0
Start_x=0.45 end_x=1.00 Model=Band_gap terms=1.424,-1.53,0.45,0,0

ELECTRON_AFFINITY Value=4.07,0.83
```

```
STATIC_PERMITIVITY Value=12.9,1.53,0.67

REFRACTIVE_INDEX Value=3.3,0.21

#Absorbtion is same as GaAs with no alloy
ABSORPTION Segments=6
start_e=0 end_e=g value=0
start_e=g end_e=g+1 value=2.698e3+8.047e4*(e-g)-6.241e4*(e-g)^2+7.326e4*(e-g)^3
start_e=g+1 end_e=g+1.4 value=-3.218e6+9.060e6*(e-g)-8.428e6*(e-g)^2+2.681e6*(e-g)^3
start_e=g+1.4 end_e=g+1.9 value=-1.615e7+2.600e7*(e-g)-1.338e7*(e-g)^2+2.303e6*(e-g)^3
start_e=g+1.9 end_e=g+2.6 value=8.383e5+2.442e5*(e-g)-3.226e5*(e-g)^2+8.482e4*(e-g)^3
start_e=g+2.6 end_e=g+4.0 value=7.83e5

THERMAL_CONDUCTIVITY Model=Thermal_Conduct terms=1,2.27,73.43,-72,0
DERIV_THERMAL_CONDUCT Model=Thermal_Conduct terms=-1,2.27,73.43,-72,0

ELECTRON_MOBILITY  Value=8500,-17700,49200

HOLE_MOBILITY Value=300

ELECTRON_DOS_MASS Value=.063,-.043,.003

HOLE_DOS_MASS Value=0.51,-0.1

ELECTRON_COND_MASS Value=.063,-.043,.003

HOLE_COND_MASS Value=0.51,-0.1

#All the parameters are the same as the default GaAs and the Al alloy of GaAs

ELECTRON_SHR_LIFETIME Value=1e-8

HOLE_SHR_LIFETIME Value=1e-8

ELECTRON_AUGER_COEFFICIENT Value=1.5e-31
QW_ELECTRON_AUGER_COEFFICIENT Value=1.5e-19

HOLE_AUGER_COEFFICIENT Value=1.5e-31
QW_HOLE_AUGER_COEFFICIENT Value=1.5e-19

RAD_RECOMB_CONST Value=1.5e-10

ELECTRON_ENERGY_LIFETIME Value=1.e-12
HOLE_ENERGY_LIFETIME Value=1.e-12

QW_RAD_RECOMB_CONST Value=1.54e-4

ELECTRON_COLLISION_FACTOR Value=0.5
HOLE_COLLISION_FACTOR Value=0.5
```

6.2 Variable Angle Spectroscopic Ellipsometry Results

As outlined in Section 2.3.1, variable angle spectroscopic ellipsometry (VASE) measurements were performed on the samples with designed Indium contents of 5%, 10%, and 15%. Each epi wafer was measured at three angles of incidence: 65, 70, and 75 degrees. The complete results are included below.

6.2.1 5% Sample

MSE=1.746

Thick.3	2.3546±0.0371
Angle0	65.507±0.0377
Thick.1	57.854±5.13
Alloy.1	0.064526±0.0132
Thick.2	99.248±2.61
Angle1	70.535±0.0271
Angle2	75.549±0.0179

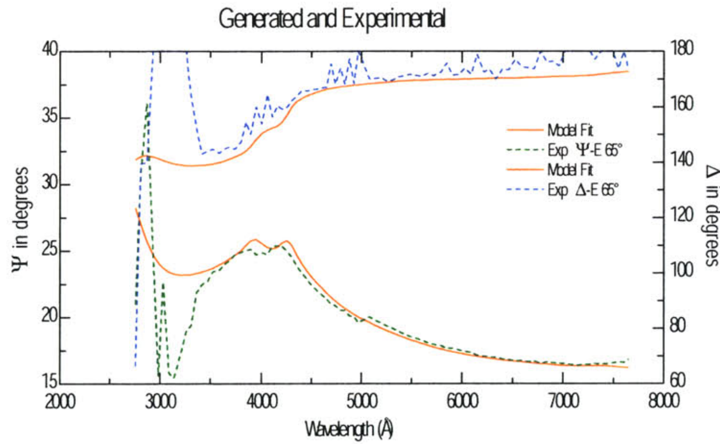

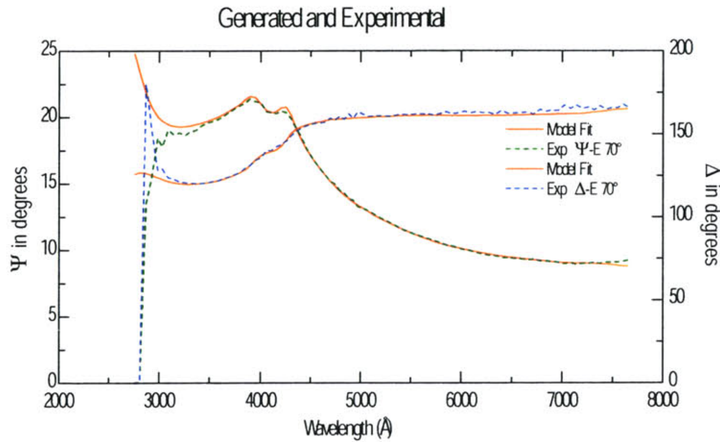

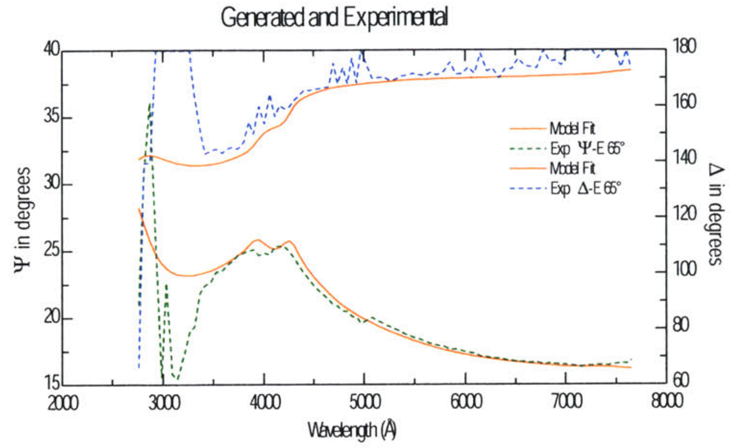

6.2.2 10% Sample

MSE=1.287

Thick.3	2.2666±0.0247
Angle0	65.476±0.0175
Thick.1	59.84±1.85
Alloy.1	0.11482±0.00995
Thick.2	102.82±0.927
Angle1	70.49±0.0156
Angle2	75.441±0.015

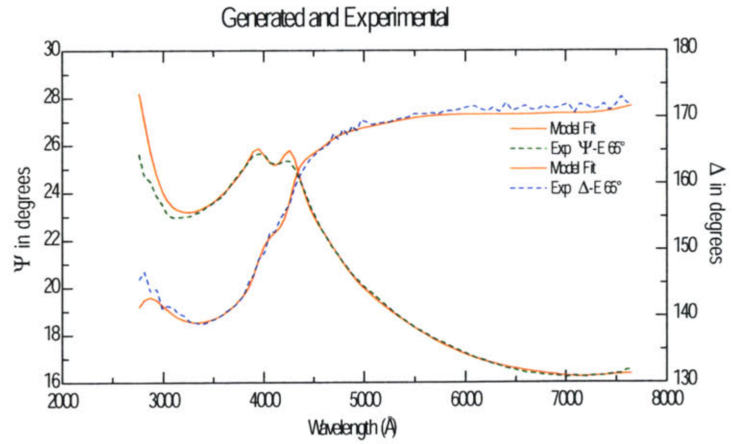

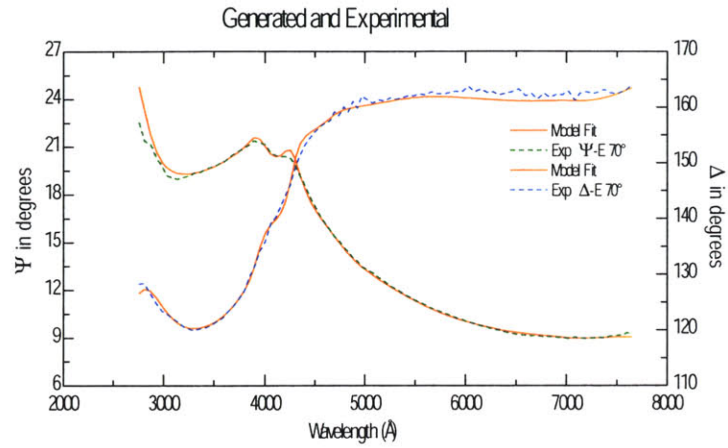

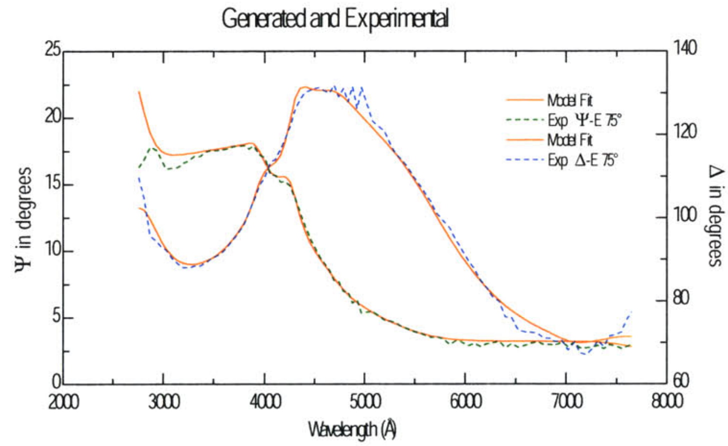

6.2.3 15% Sample

MSE=1.321

Thick.3	2.1751±0.0355
Angle0	65.316±0.0192
Thick.1	59.917±1.98
Alloy.1	0.13546±0.0134
Thick.2	105.4±0.992
Angle1	70.411±0.0259
Angle2	75.577±0.0193

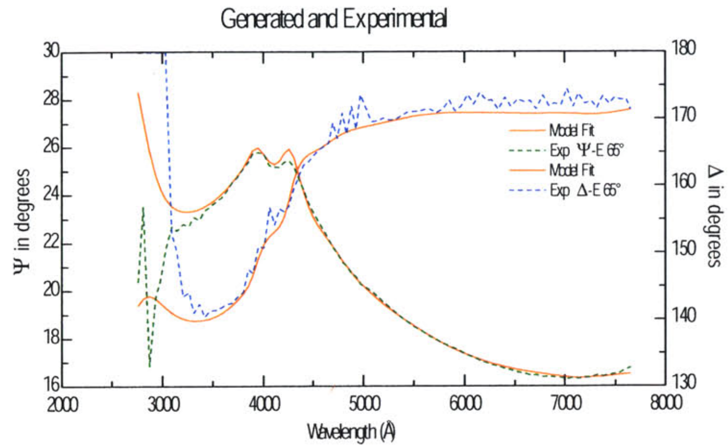

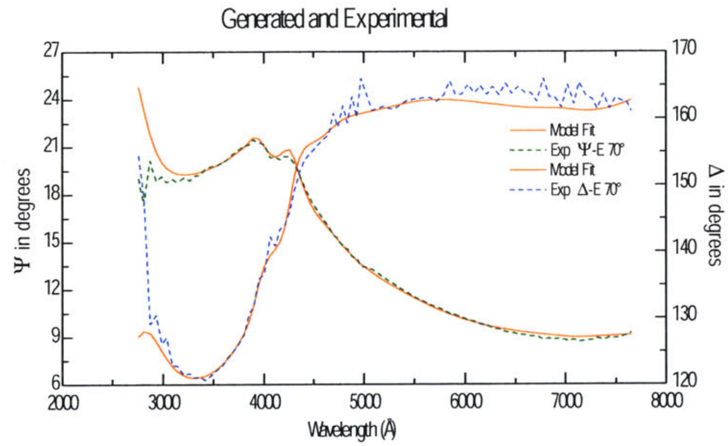

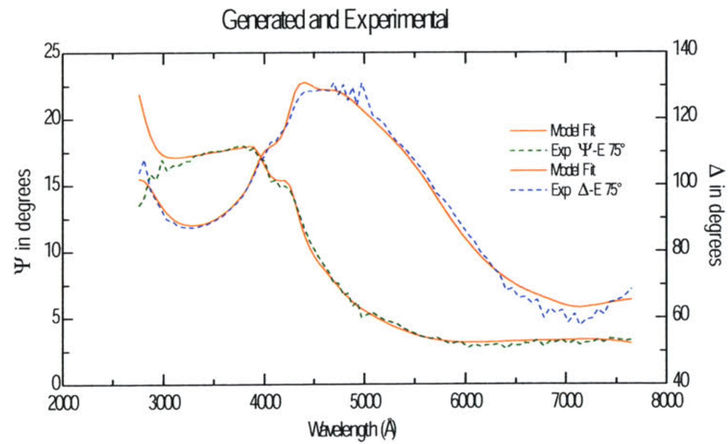

3382-115